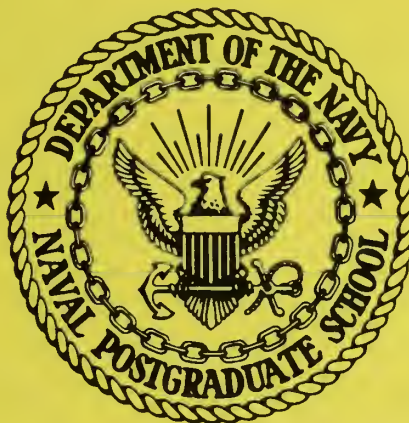


NPS-57Nt75101

NAVAL POSTGRADUATE SCHOOL

Monterey, California



AN INVESTIGATION OF THE FLOW
IN
TURBOJET TEST CELLS AND AUGMENTERS

by

Jack D. Hayes and David W. Netzer

October 1975

Approved for public release; distribution unlimited

Prepared for:
Naval Air Propulsion Test Center
Trenton, NJ

FEDDOCS
D 208.14/2:NPS-57NT75101

NAVAL POSTGRADUATE SCHOOL

Monterey, California

Rear Admiral I. W. Linder

Jack R. Borsting

Superintendent

Provost

The work reported herein was supported by the Naval Air Propulsion Test Center, Trenton, New Jersey, and was a part of the Naval Environmental Protection Data Base Program.

Reproduction of all or part of this report is authorized.

This report was prepared by:

UNCLASSIFIED

SECURITY CLASSIFICATION OF THIS PAGE (When Data Entered)

REPORT DOCUMENTATION PAGE		READ INSTRUCTIONS BEFORE COMPLETING FORM
1. REPORT NUMBER NPS-57Nt-75101	2. GOVT ACCESSION NO.	3. RECIPIENT'S CATALOG NUMBER
4. TITLE (and Subtitle) An Investigation of the Flow in Turbojet Tests Cell and Augmenters		5. TYPE OF REPORT & PERIOD COVERED Interim
		6. PERFORMING ORG. REPORT NUMBER
7. AUTHOR(s) Jack Douglas Hayes and David W. Netzer		8. CONTRACT OR GRANT NUMBER(s)
9. PERFORMING ORGANIZATION NAME AND ADDRESS Naval Postgraduate School Monterey, California 93940		10. PROGRAM ELEMENT, PROJECT, TASK AREA & WORK UNIT NUMBERS N623765WR00037
11. CONTROLLING OFFICE NAME AND ADDRESS Naval Air Propulsion Test Center Trenton, New Jersey		12. REPORT DATE October 1975
		13. NUMBER OF PAGES 85
14. MONITORING AGENCY NAME & ADDRESS (if different from Controlling Office)		15. SECURITY CLASS. (of this report) Unclassified
		15a. DECLASSIFICATION/DOWNGRADING SCHEDULE
16. DISTRIBUTION STATEMENT (of this Report) Approved for public release; distribution unlimited.		
17. DISTRIBUTION STATEMENT (of the abstract entered in Block 20, if different from Report)		
18. SUPPLEMENTARY NOTES		
19. KEY WORDS (Continue on reverse side if necessary and identify by block number) Turbojet Test Cell Augmenter Flow Model		
20. ABSTRACT (Continue on reverse side if necessary and identify by block number) A two-dimensional elliptic computer model was adapted to the solution of the flow field in a turbojet test cell section which contained the engine exhaust duct and augmentor tube. Various engine power settings, augmentation ratios, and augmentor geometries were investigated. Flow visualization and static pressure recovery were		

DD FORM 1 JAN 73 1473

EDITION OF 1 NOV 65 IS OBSOLETE
S/N 0102-014-6601

3

Unclassified
SECURITY CLASSIFICATION OF THIS PAGE (When Data Entered)

UNCLASSIFIED

SECURITY CLASSIFICATION OF THIS PAGE(When Data Entered)

(20. ABSTRACT)

primary objectives subject to specified engine power settings and augmentation ratios. Capabilities and limitations of the model are discussed.

TABLE OF CONTENTS

I.	INTRODUCTION -----	11
A.	BACKGROUND -----	11
B.	TEST CELL POLLUTION -----	13
C.	SCOPE OF STUDY -----	14
II.	THEORETICAL APPROACH -----	16
III.	MODEL DISCUSSION -----	22
A.	COORDINATE SELECTION -----	22
B.	GEOMETRY -----	22
C.	GRID SPACING -----	23
D.	BOUNDARY CONDITIONS -----	24
1.	Engine Exhaust Duct -----	24
a.	Stream Function -----	24
b.	Vorticity -----	24
c.	Mass Fraction/Temperature -----	24
d.	Turbulence Kinetic Energy -----	24
e.	Turbulence Energy Dissipation Rate -	26
2.	Inlet to Cell -----	26
a.	Stream Function/Velocity -----	26
b.	Vorticity -----	26
c.	Mass Fraction/Temperature -----	27
d.	Turbulence Kinetic Energy -----	27
e.	Turbulence Dissipation -----	27
3.	Solid Boundaries -----	27
a.	Velocity/Stream Function -----	27
b.	Vorticity -----	28
(1)	Laminar Case -----	28

	(2) Turbulent Case -----	29
	(3) Special Points -----	30
	c. Turbulence Kinetic Energy -----	32
	d. Turbulence Dissipation -----	33
	e. Temperature/Mass Fraction -----	33
	4. Augmenter Exit -----	33
	5. Geometric Centerline -----	33
	E. INITIAL CONDITIONS -----	34
	F. SOLUTION PROCEDURES -----	34
IV.	MODEL DEVELOPMENT -----	36
	A. GRID SPACING -----	36
	B. CONVERGENCE CRITERIA -----	37
	C. PLOTTING PACKAGE -----	37
V.	PARAMETRIC STUDY -----	38
VI.	RESULTS AND DISCUSSION -----	41
	A. FLOW CONDITION 1. -----	41
	1. Streamlines/Temperature Contours -----	41
	2. Pressure Recovery -----	43
	a. Axial (z-direction) -----	43
	b. Radial (R-direction) -----	44
	c. Total Axial Static Pressure Rise ---	44
	B. FLOW CONDITION 2. -----	45
	C. FLOW CONDITION 3. -----	47
	D. FLOW CONDITION 4. -----	47
	E. FLOW CONDITION 5. -----	48
	F. FLOW CONDITION 6. -----	48

VII. CONCLUSIONS AND RECOMMENDATIONS -----	50
A. CONCLUSIONS -----	50
B. RECOMMENDATIONS -----	50
LIST OF REFERENCES -----	81
INITIAL DISTRIBUTION LIST -----	82

LIST OF TABLES

I.	Coefficient Values -----	18
II.	Flow Conditions -----	39
III.	TF-41 Test Conditions -----	40

LIST OF FIGURES

1.	Typical Turbojet Test Cell -----	52
2.	TF-41 Test Configuration -----	53
3a.	Computer Model Geometry: Flow Condition 1 -----	54
3b.	Computer Model Geometry: Flow Condition 3 -----	55
3c.	Computer Model Geometry: Flow Condition 4 -----	55
3d.	Computer Model Geometry: Flow Condition 5 -----	55
4.	Velocity Profiles in Inlet Flows -----	56
5.	Identification of Boundaries -----	56
6.	Laminar Sublayer Velocity Profile -----	56
7.	Grid Line Locations for Pressure Calculations -----	57
8a.	Streamline Contours: Flow Condition 1 -----	58
8b.	Temperature Contours: Flow Condition 1 -----	59
8c.	Axial Pressure Gradients: Flow Condition 1 (Lines A-A and B-B) -----	60
8d.	Axial Pressure Gradients: Flow Condition 1 (Lines C-C and D-D) -----	61
8e.	Axial Pressure Gradients: Flow Condition 1 (Line E-E) -----	62
8f.	Radial Pressure Gradient: Flow Condition 1 (Line G-F) -----	63
8g.	Radial Static Pressure Variations: Flow Condition 1 (Line G-F) -----	63
8h.	Axial Static Pressure Variations: Flow Condition 1 (Lines A-A and B-B) -----	64
8i.	Axial Static Pressure Variations: Flow Condition 1 (Lines C-C thru E-E) -----	65
8j.	ΔP Rise Versus Number of Iterations: Flow Condition 1 -----	66

9a.	ΔP Rise Versus Augmentation Ratio: Flow Condition 1 -----	67
9b.	Streamline Contours: Flow Condition 2 (AR = 1.0) -----	68
9c.	Temperature Contours: Flow Condition 2 (AR = 1.0) -----	69
10a.	Streamline Contours; Flow Condition 3 (Small Augmenter Inlet Radius) -----	70
10b.	Temperature Contours; Flow Condition 3 (Small Augmenter Inlet Radius) -----	71
10c.	Streamline Contours; Flow Condition 3 (Large Augmenter Inlet Radius) -----	72
10d.	Temperature Contours; Flow Condition 3 (Large Augmenter Inlet Radius) -----	73
11a.	Streamline Contours: Flow Condition 4 -----	74
11b.	Temperature Contours: Flow Condition 4 -----	75
12a.	Streamline Contours: Flow Condition 5 -----	76
12b.	Temperature Contours: Flow Condition 5 -----	77
13a.	Streamline Contours: Flow Condition 6 -----	78
13b.	Temperature Contours: Flow Condition 6 -----	79
13c.	ΔP Rise Versus Number of Iterations: Flow Condition 6 -----	80

I. INTRODUCTION

A. BACKGROUND

Jet engines undergoing maintenance are tested in jet engine test cells prior to their operational use. A typical test cell is shown in Figure 1 and can be viewed as a "U" shaped concrete structure of rectangular cross-section. The cell is designed to provide clean distortion free airflow to the engine inlet, which is necessary for accurate performance evaluation. In addition, the cell attenuates noise and provides safety for test equipment and personnel.

Engine exhaust is directed into an augments tube, then deflected vertically to be expelled into the atmosphere. The augments tube acts in combination with engine exhaust momentum to form a jet pump. In reality, the engine exhaust jet entrains secondary air (air not ingested by the engine) which is then carried through the augments tube by exhaust jet momentum. Frictional losses associated with the mass of air moving through the test cell are thus overcome by the jet pump's energy addition.

The quantity of secondary air entrained is crucial to proper engine testing. Too little entrainment allows exhaust gas recirculation to the engine inlet. Too much entrainment causes excessive static pressure gradients to exist between engine inlet and exhaust planes. Static pressure should be nearly identical in both planes for proper testing but a

small gradient must exist to prevent exhaust gas recirculation. Sufficient secondary air should be entrained to cool the engine exhaust to acceptable levels. Also, exhaust flow with very high kinetic energy can damage the test cell; secondary air entrainment reduces this energy.

Augmentation ratio is defined as the ratio of entrained secondary air to the jet exhaust mass flow (primary flow). In practice, engine/augmenter tube separation is adjusted to generate sufficient secondary flow to prevent exhaust gas recirculation at all power settings. Occasionally, the augmenter inlet diameter is varied to further control the entrainment process.

Both analytical and empirical methods have been applied to the entrainment mixing problem. Empirical equations are usually applied to particular test cells, but operator experience coupled with trial and error are required to create the desired secondary flow.

Larger and more expensive test cells are needed in the future to replace obsolete cells and to accommodate new engines with greatly increased mass flow rates. Present design tools do not adequately describe the flow field in a test cell and new design concepts cannot be evaluated until the cells are constructed. An accurate flow model would provide a needed design tool and would help prevent costly design errors.

B. TEST CELL POLLUTION

Test cell installations are becoming increasingly subjected to localized state and community pollution control board regulations. The occasional prominent exhaust plume rising from test cells is a continual source of local complaint. Even when the plume is not visible, the cell emits pollutants similar to those of aircraft operating in the area.

Fortunately, the stationary cell is amenable to exhaust treatment which has been shown to be effective in reducing particulate emissions to acceptable levels. The cost associated with the construction and operation of the necessary equipment is high and is a function of total mass flow (primary plus secondary) through the cell. Thus, it is necessary to minimize total mass flow to minimize abatement costs.

Carbon particulates and unburned hydrocarbons are of immediate concern in the abatement of emissions from jet test cells. Also of concern are nitrogen oxides (NO_x), carbon monoxide (CO) and sulfur dioxide. The amount of each pollutant emitted is a function of engine type and mechanical condition. Power setting alters emissions with CO and unburned hydrocarbons predominate at idle. Particulates and nitrogen oxides are the main pollutants at high power settings. Afterburner operation provides very high external exhaust temperatures and chemical reactions continue as the flow passes into

the augments tube. The secondary air mixing is believed to alter chemical reaction rates by effectively quenching portions of the exhaust jet. Present flow models do not describe the process completely and it has not been possible until recently to accurately measure mass emission factors in the afterburner core due to the high temperatures and the chemical kinetic nature of the process.

To fully optimize the pollution abatement method it is necessary to understand how exhaust pollutants are formed, in what quantities and at what rates. The effect of engine power setting and secondary flow entrainment on emitted pollutants must also be analyzed. Pollutant measurement would be simpler and less costly if accurate species and velocity distribution predictions could be made at specified points in the test cell exhaust system. To accomplish these tasks, more complete knowledge of the air flow through test cells must be acquired.

C. SCOPE OF STUDY

Most analysis for predicting dilution air is very empirical, usually requiring an empirical jet spread equation. Recent advances have been made toward solving the recirculating, turbulent fluid flow problem. One technique is due to Spalding et al. [Refs. 1 and 2]. The governing two-dimensional elliptic partial differential equations are reduced to finite difference equations and solved by numeric methods.

Air flow through a test cell is known to be turbulent and does possess regions of recirculation. The purpose of this study was to apply the methods described by Spalding to the flow field encompassing the engine exhaust and augmentor tube of a typical Navy jet engine test cell.

Flow visualization and static pressure recovery were primary objectives of this study. Parametric studies were made which involved the variation of augmentor geometry, engine power setting, augmentation ratio and cell inlet flow conditions.

The study was restricted to non-afterburning, subsonic engine exhaust conditions.

II. THEORETICAL APPROACH

Two-dimensional fluid flow with regions of reverse-flow can be described mathematically by second-order elliptic partial differential equations. These equations can be reduced to "finite-difference" non-linear algebraic equations and solved simultaneously by an iterative procedure. One such procedure is detailed by Spalding and others in References 1 and 2 and was the method used in this study.

The conservation of mass, momentum and energy are the fundamental equations used in the problem formulation. The dependent variables chosen by Spalding et al. [1,2] are stream functions (ψ) and vorticity (ω) to assure mass and momentum conservation. Temperature was used as the dependent variable for energy conservation since the flow was considered inert. Since the velocities under consideration were low, kinetic heating was ignored. Specific heat was considered to be constant.

Although pressure and, to a large extent, velocity are removed from the formulation, they can easily be "backed-out" of the vorticity and stream functions solutions respectively.

A turbulence model is needed in order to provide "effective" transport properties. The Jones-Launder turbulence model [2,3] is used to describe the variation of the effective viscosity, μ_{eff} . Two variables are used in this model: turbulence kinetic energy, K and turbulence

energy dissipation rate, ϵ . The model is a time-averaged turbulence model and the two associated differential equations can be cast in elliptic form. Thus, the solution procedure for ψ , ω and T also applies to K and ϵ . The relationship between K and ϵ is:

$$\mu_{\text{eff}} = C_{\mu} \rho \frac{K^2}{\epsilon}$$

where

$$\rho = \text{local density}$$

$$C_{\mu} = \text{empirically determined coefficient} = 0.09$$

These five equations together with the equation of state for a perfect gas describe the complete flow field. Choosing cylindrical coordinates (R, θ, z) allows all five equations to be written in the following general form:

$$\begin{aligned} a_{\phi} \left[\frac{\partial}{\partial z} \left(\phi \frac{\partial \psi}{\partial R} \right) - \frac{\partial}{\partial R} \left(\phi \frac{\partial \psi}{\partial z} \right) \right] - \frac{\partial}{\partial z} \left[b_{\phi} R \frac{\partial (c_{\phi} \phi)}{\partial z} \right] \\ - \frac{\partial}{\partial R} \left[b_{\phi} R \frac{\partial (c_{\phi} \phi)}{\partial R} \right] + R S_{\phi} = 0 \end{aligned}$$

where ϕ stands for ψ , $\frac{\omega}{R}$, T , K , or ϵ . The functions a_{ϕ} , b_{ϕ} , c_{ϕ} and S_{ϕ} are given in Table I.

TABLE I
COEFFICIENT VALUES

ϕ	a	b	c	s
$\frac{\omega}{R}$	R^2	R^2	μ_{eff}	$S_{(\omega/R)}$
ψ	0	$\frac{1}{\rho R^2}$	1	$-\frac{\omega}{R}$
K	1	$\frac{\mu_{\text{eff}}}{\sigma_K}$	1	$-(G - \rho\epsilon)$
ϵ	1	$\frac{\mu_{\text{eff}}}{\sigma_\epsilon}$	1	$-(\frac{c_1 G \epsilon}{K} - \frac{c_2 \rho \epsilon^2}{K})$
T	1	$\frac{\mu_{\text{eff}}}{\sigma_h}$	1	0

where

$$\sigma_K \equiv \frac{\mu_{\text{eff}}}{\Gamma_{K,\text{eff}}} \quad \text{taken to be 1.0}$$

$\Gamma_{K,\text{eff}} \equiv$ the exchange coefficient of the kinetic energy of the fluctuating motion, K.

$$\sigma_E \equiv \frac{\mu_{eff}}{\Gamma_{\epsilon,eff}} \quad \text{taken to be 1.3}$$

$\Gamma_{\epsilon,eff}$ the exchange coefficient of the turbulence energy dissipation rate, ϵ .

$$\sigma_H \equiv \frac{\mu_{eff}}{\Gamma_{h,eff}} \quad \text{taken to be 1.0}$$

$\Gamma_{h,eff}$ the exchange coefficient of heat

$$G \equiv \mu_{eff} \left\{ 2 \left[\left(\frac{\partial V_z}{\partial z} \right)^2 + \left(\frac{\partial V_R}{\partial R} \right)^2 + \left(\frac{V_R}{R} \right)^2 \right] + \left(\frac{\partial V_z}{\partial R} + \frac{\partial V_R}{\partial z} \right)^2 \right\}$$

c_1 and c_2 are empirically determined coefficients.

$$(c_1 = 1.45, c_2 = 2.0)$$

Neglecting tangential momentum, the vorticity source term

$S_{(\omega/R)}$ is

$$S_{(\omega/R)} = -R \left[\frac{\partial}{\partial z} \left(\frac{V_z^2 + V_R^2}{2} \right) \frac{\partial \rho}{\partial R} - \frac{\partial}{\partial R} \left(\frac{V_z^2 + V_R^2}{2} \right) \frac{\partial \rho}{\partial z} \right] + \text{negligible terms}$$

The first term of the general equation is the convective term while the second and third terms are the diffusion terms. The last term is the source term which includes all terms not strictly convective or diffusive.

Once the equations are solved and a converged solution is acquired, the static pressure distribution in the flow field can be calculated by integrating the momentum equation in the axial or radial direction. The resultant equation for the gradient in the axial (z) direction is

$$\begin{aligned} \frac{\partial P}{\partial z} = & \frac{\partial}{\partial z} \left\{ \mu_{\text{eff}} \left[2 \frac{\partial V_z}{\partial z} - \frac{2}{3} \text{div } \vec{V} \right] - \rho V_z^2 \right\} \\ & + \frac{1}{R} \frac{\partial}{\partial R} \left\{ R \mu_{\text{eff}} \left[\frac{\partial V_z}{\partial R} + \frac{\partial V_R}{\partial z} \right] - R \rho V_z V_R \right\} \end{aligned}$$

The analogous form in the radial (R) direction (neglecting θ -momentum) is

$$\begin{aligned} \frac{\partial P}{\partial R} = & \frac{1}{R} \left\{ -\mu_{\text{eff}} \left(\frac{2V_R}{R} - \frac{2}{3} \text{div } \vec{V} \right) \right\} \\ & + \frac{\partial}{\partial z} \left\{ \mu_{\text{eff}} \left(\frac{\partial V_z}{\partial R} + \frac{\partial V_R}{\partial z} \right) - \rho V_z V_R \right\} \\ & + \frac{1}{R} \frac{\partial}{\partial R} \left\{ R \mu_{\text{eff}} \left[2 \frac{\partial V_R}{\partial R} - \frac{2}{3} \text{div } \vec{V} \right] - R \rho V_R^2 \right\} \end{aligned}$$

where

$$\text{div } \vec{V} = \frac{\partial V_z}{\partial z} + \frac{1}{R} \frac{\partial (R V_R)}{\partial R}$$

Pressure is then obtained by the following approximate integration formula:

$$\int_A^B \frac{\partial P}{\partial z} dz \approx \frac{1}{2} \left[\left(\frac{\partial P}{\partial z} \right)_A + \left(\frac{\partial P}{\partial z} \right)_B \right] (z_B - z_A)$$

III. MODEL DISCUSSION

A. COORDINATE SELECTION

Although the test cell cross-section is basically rectangular, the engine exit and augments tube can be accurately described using two-dimensional axi-symmetrical flow. Of primary interest is the mixing of the engine exhaust (primary flow) and ambient air (secondary flow). This process primarily occurs between the two circular "tubes" and within the augments tube. Reference 4 suggests that test cell wall proximity will influence primary/secondary flow mixing. However, the large dimensions of the cell compared with the engine and augments diameters should allow the use of cylindrical coordinates with little error.

B. GEOMETRY

Figure 1 is a profile view of a test cell located at NARF Alameda, used to test TF-41 engines. Figure 2 is the geometry established for an engine test while Figure 3 is the geometry used in this study. The actual dimensions are easily varied in the computer program allowing parametric studies to be made to assess the effects of geometry change on the flow field. The field is assumed axi-symmetric although in practice the engine/augments combination is located nearer the test cell floor than the walls or ceiling. The cell ceiling is modeled as cylindrical but in actuality is quite flat.

To minimize the number of grid points required in the axial (z) direction, the cell "inlet" was located a few feet upwind of the engine exhaust.

The straight augmenter duct "lip" used in the computer model was a necessary simplification to the beveled lip since grid points in the coordinate system lie along mutually perpendicular grid lines. Augmenter tubes in Navy test cells are by no means uniform in design and inlet shapes vary greatly. It is believed that a straight lip design does not greatly affect the flow analysis.

Augmenter tubes used to test afterburner operation usually contain quench systems and flow baffles. These were not considered in this analysis.

C. GRID SPACING

Various grid sizes were used to appraise the effect of grid size on the predicted flow field. The largest number of grid points was described by a 60x50 (zxR) matrix and the smallest by a 20x25 matrix. Regardless of the size of the grid, every boundary must be defined by a grid line. In general, grid line separation should be smaller as one approaches a wall since gradients in properties are large in this region.

Spalding [1,2] suggests that in the region of solid boundaries each succeeding grid spacing not differ from the last by more than a factor of 1.5.

D. BOUNDARY CONDITIONS

All dependent variables must be specified in some manner on the boundaries. The boundaries of this model include: (1) the engine exhaust duct, (2) the cell inlet, (3) the solid boundaries, (4) the augments outlet, and (5) the geometric centerline.

1. Engine Exhaust Duct

a. Stream Function/Velocity

Plug flow was assumed at the engine exhaust plane. The axial velocity distribution is uniform (Figure 4) to produce a specified mass flow and no radial component of velocity exists.

b. Vorticity

Since no velocity gradients exist, vorticity is identically zero.

c. Mass Fraction/Temperature

A non-dimensional mass fraction/temperature was assigned a value of 1.0 at the engine exit. This corresponds to the actual exhaust temperature existing at the specified power setting.

d. Turbulence Kinetic Energy

Kinetic energy of turbulent motion (K) is defined by

$$K = \frac{1}{2} (\overline{v_R^2} + \overline{v_\theta^2} + \overline{v_z^2})$$

where $v_{()}$ are the instantaneous fluctuations in free stream velocity.

For isotropic turbulence the expression for K can be written $K = \frac{3}{2} \overline{v^2}$.

Intensity of turbulence is defined as

$$I = \frac{\sqrt{\frac{1}{3} (\overline{v_R^2} + \overline{v_\theta^2} + \overline{v_z^2})}}{\bar{V}}$$

Assuming isotropic turbulence

$$I = \frac{\sqrt{\overline{v^2}}}{\bar{V}}$$

where \bar{V} is the mean flow velocity.

Spalding [1,2] presents an empirical relation for K in uniform flow:

$$K = 0.004 (\bar{V})^2$$

Setting

$$\frac{3}{2} \overline{v^2} = .004 (\bar{V})^2$$

and substituting into the intensity relation we find

$$I = \frac{\sqrt{\frac{.008}{3} \bar{V}^2}}{\bar{V}} = 0.052$$

Schlichting [5] experimentally determined intensity values of between 0.05 and 0.08 in low subsonic wind tunnel flow. Thus, it appears Spalding's relation is adequate for estimating K in the engine exit and was utilized as the boundary condition.

e. Turbulence Energy Dissipation Rate

K and ϵ are related through the dissipation length scale ℓ [2] by

$$\epsilon = \frac{K^{3/2}}{\ell}$$

In this program ℓ was taken to be:

$$\ell = 0.022 \times (\text{Engine Radius})$$

2. Inlet to Cell

a. Stream Function/Velocity

A linear variation of inlet axial velocity was chosen which varied from a positive value at the engine wall to zero at the cell ceiling to produce a specified secondary mass flow (Figure 4). No specific information was available to specify this flow distribution accurately. Lacking more specific information, the radial components of velocity (V_R) were fixed at zero.

b. Vorticity

Vorticity was computed using

$$\frac{\omega}{R} = \frac{1}{R} \left(\frac{\partial V_R}{\partial z} - \frac{\partial V_z}{\partial R} \right)$$

c. Mass-Fraction/Temperature

Non-dimensional temperature and mass-fraction were assigned a value of 0.0 at the cell inlet. This corresponded to an actual temperature of 520 °R.

d. Turbulent Kinetic Energy (K)

K was specified at each grid point using the expression

$$K = 0.004 \bar{V}^2$$

Where \bar{V}^2 is the local flow velocity.

e. Turbulence Dissipation

$$\epsilon = K^{3/2}/\ell$$

$$\ell = 0.022 \times (\text{Cell Radius} - \text{Engine Radius})$$

3. Solid Boundaries

There are eight solid boundaries described in the present model. Each is numbered in Figure 5 for reference. Two are engine surfaces, two are cell walls and four describe the augments tube.

a. Velocity/Stream Function

Along the engine surfaces (1 and 2, Figure 5) stream function is constant and determined from the specified mass flow through the engine. The remaining solid boundaries

have the stream function fixed at a value which is the sum of the engine mass flow and cell inlet mass flow. All velocities at a solid boundary are zero.

b. Vorticity

Vorticity near a solid boundary was computed in one of two ways depending on the magnitude of the local grid cell Reynolds number.

(1) Laminar Sublayer Case. If the local grid cell Reynolds number ($R \equiv \Delta\psi/\mu R$) is found to be less than 290 [1,2], a linear velocity gradient is assumed. Using the additional assumption that the velocity gradient in the direction perpendicular to the wall is much greater than the gradient parallel to the wall, the vorticity is calculated using the vorticity definition and discarding the parallel term. For example, given a wall parallel to the horizontal (z) axis with flow in the positive z-direction, the vorticity would be found by:

$$\omega = \frac{\partial V_R}{\partial z} - \frac{\partial V_z}{\partial R} \approx - \frac{\partial V_z}{\partial R} = - \frac{\Delta V_z}{\Delta R} = - \frac{V_p}{\Delta R}$$

where $\frac{\partial V_R}{\partial z}$ is considered small. V_p is the velocity in the z-direction at node P (Figure 6). Since velocity at the wall is zero, it is easily seen that V_p is twice the average velocity between the wall and the nearest grid point off the wall. This is convenient since the average velocity is related to the stream function by

$$V_{z_{avg}} = \frac{V_P}{2} = \frac{1}{\rho R} \frac{\Delta \psi}{\Delta R}$$

and the local Reynolds number is

$$Re \equiv \frac{\Delta \psi}{\mu \frac{R}{\rho}}$$

Therefore, the vorticity expression is given by

$$\omega = - \frac{\Delta V_z}{\Delta R} = - \frac{V_P}{\Delta R} = \frac{2 Re \mu}{\rho (\Delta R)^2}$$

which is easily calculated.

(2) Turbulent Case. When the local grid cell Reynolds number at the near wall node exceeds 290 the flow is considered turbulent. Vorticity is then defined as

$$\omega = \frac{\tau_{shear}}{\mu_{wall}}$$

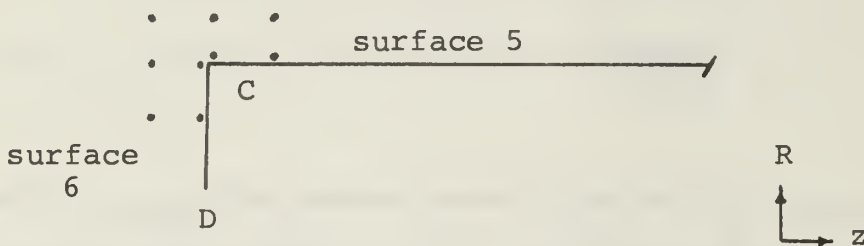
where τ_{shear} is the wall shear stress and μ_{wall} is the viscosity on the wall. τ_{shear} is given by the relation:

$$\tau_{shear} = \frac{C_f}{2} \rho \bar{V}^2$$

The coefficient $(\frac{C_f}{2})$ was calculated using

$$\frac{C_f}{2} = \frac{.0284}{Re^{.25}}, \quad \text{where } Re = \frac{\Delta \psi}{\mu \frac{R}{\rho}}$$

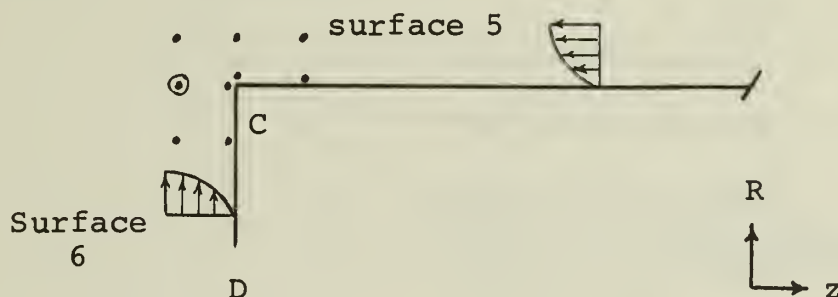
(3) Special Points. The preceding discussion of vorticity calculation near solid boundaries assumed a well-developed boundary layer. There are locations in the field where the fluid may meet a parallel solid surface and the vorticity calculation becomes suspect. Such a point is the intersection of surface 5 and surface 6 of Figure 5 (point C). There are two problems associated with this point. If the flow is predominantly in the positive z -direction, a fully developed boundary layer will not exist on surface 5 at point C. If the flow is in the negative R -direction near surface 6, the identical problem arises. Also, each surface (5 and 6) will have a unique value of vorticity at point C and it is necessary to keep them properly identified in the computer program (see sketch below).



No completely satisfactory numerical method exists in this scheme to account for the singularity. Initial computer runs were made allowing the vorticity at point C to be calculated as if a fully developed boundary layer existed on both surfaces (5 and 6). Converged solutions resulted with realistic flow visualizations around this point

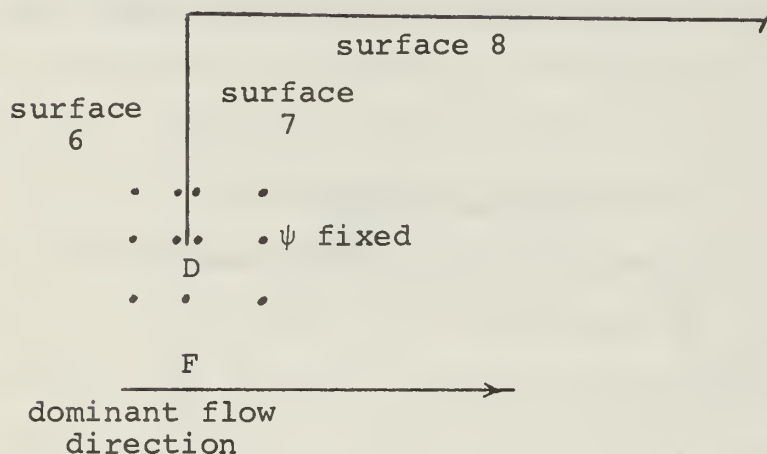
as long as a recirculation region did not develop on the augmeter duct lip (surface 6).

When flow developed in the positive R-direction near surface 6 with negative z-direction flow on surface 5, the solution would not converge and often diverged (see sketch below).



References 1 and 2 state that special attention must be paid to points which define enlargements in pipe flow (Points A and D of Figure 5). In order to obtain realistic jet spread, stream function must be fixed on the node immediately downwind of these points. It became evident that the flow would usually be in the negative z-direction along surface 5, so ψ was fixed at the node circled in the sketch above. This solved the divergence problem occurring under certain flow conditions, and appeared not to alter the solution appreciably. Point D is unusual in that it defines the end of an "infinitely thin" wall. It also defines an "enlargement" and for this reason, the immediate

downward ψ value was fixed at the value assigned to point D.



For purposes of calculating the vorticity at node F (see above sketch), the vorticity at point D was taken to be the average of the vorticities computed on surface 6 and 7 shown in the above sketch.

c. Turbulence Kinetic Energy

Turbulent flow produces steep gradients of all transport properties near walls. To reduce the required number of grid points and to reduce computation time a "slip value" of turbulence kinetic energy (K) is calculated on the wall. The "slip value" is fixed to produce an arithmetic-mean gradient between the wall and adjacent node, which equals the gradient of the Couette flow solution midway between the nodes. A complete discussion of this method can be found in References 1 and 6.

d. Turbulence Dissipation

The effective boundary for turbulence dissipation (ϵ) is taken to be the n grid points adjacent to the wall. Wolfshtein [6] presents the value at the near-wall node as:

$$\epsilon_p = \left(\frac{c_\mu}{a_\mu}\right) (K_p)^{3/2} / \Delta R$$

where ϵ_p = near-wall value

c_μ = empirical constant = 0.09

a_μ = empirical constant = 0.22

K_p = near-wall turbulence kinetic energy value

ΔR = wall to near-wall node distance

e. Temperature/Mass Fraction

All solid boundaries were assumed adiabatic and, of course, impermeable. Therefore, no gradients in temperature or mass fraction existed between the walls and near-wall nodes.

4. Augmenter Exit

Axial gradients of all dependent variables were taken as zero.

5. Geometric Centerline

Radial gradients of ω/R , K , ϵ , T and mass fraction are taken as zero. Also the centerline is the stream function ($\psi = 0$) reference line.

E. INITIAL CONDITIONS

The flow field must have initial values assigned to all variables. Experience is required to fill the field with compatible variables to prevent divergence in the first few iterations.

It was found that a reasonably accurate stream function distribution was essential to prevent divergence. In particular, the predominant flow direction must be established and large discontinuities in stream function should not exist. The flows in the augments tube and the free stream area between the engine exhaust and augments tube were initialized as well-developed pipe flow. This allowed compatible vorticity values to be calculated in these regions.

Density, mass fraction, viscosity, and turbulence kinetic energy were specified using reference values taken from either the cell inlet or engine exit. Turbulence dissipation was calculated using the relationship discussed under boundary conditions.

F. SOLUTION PROCEDURES

To counter computational instabilities in the first 400 iterations, stream function variation between iterations was under-relaxed by a factor of 0.3. All other variables were under-relaxed by 0.5. The relaxation parameters were increased to 0.6 and 0.8, respectively, after 400 iterations.

Various flows, geometries, and grids were investigated successfully using the above relaxation parameters. They

precluded divergence in the most unstable flow condition handled: high engine mass flow with low augmentation ratio (200 lbm/sec, 0.25, respectively). However, it should be noted that initial conditions must be well established for these relaxation parameters to be effective.

IV. MODEL DEVELOPMENT

The geometry shown in Figure 3a was chosen to represent a test cell section containing an engine exhaust nozzle and augments tube. Approximate dimensions were taken from a TF-41 turbofan engine undergoing testing at NARF Alameda.

A. GRID SPACING

A grid composed of twenty lines in the z-direction and twenty-five lines in the R-direction (20x25) was chosen to initially describe the flow field. (Intersections of mutually perpendicular grid lines define grid points.) This number of grid lines allowed the use of small grid spacing near solid walls but produced relatively large spacing away from walls.

Computation time is directly proportional to the number of grid points in the field. A small number of grid lines was chosen to minimize computer time during program debugging. Three hundred iterations typically required 7.5 minutes (excluding compile time). It should be noted that vorticity source terms were ignored during this initial period.

Vorticity source terms and pressure recovery calculations were added only after the program was successfully iterating to a converged solution. The number of grid lines was increased to 40x40 (zxR) to allow for pressure gradient calculations without the use of wall or near-wall variable values. Otherwise, large errors accumulated in the pressure integration process.

Eleven hundred iterations typically required 109 minutes of computation time (excluding compile time). This time includes one pressure calculation along eight lines in the flow field and those computations performed in the flow initialization process. However, the total time for the latter calculations amounts to less than one minute.

B. CONVERGENCE CRITERIA

Convergence rate was influenced by flow conditions, grid spacing and relaxation parameters. Two criteria were used to appraise the convergence level of the solution.

First, the percentage change in ω , ψ , K , ϵ and mass fraction (at all grid points in the field) must be arbitrarily small between successive iterations. This was done computationally by storing the largest change occurring in the field for each variable and printing that value after each iteration.

The second convergence criterion proved to be the most conclusive. That is, when pressure calculations along each grid line remained unchanged (with increased iterations) convergence was assumed.

C. PLOTTING PACKAGE

Solution values of stream function and temperature were transferred to computer cards at the conclusion of each run. These cards were then used as input to a second program which plotted streamline contours and lines of constant temperature on separate graphs. A CALCOMP Model 765 plotter was utilized for this purpose.

V. PARAMETRIC STUDY

Geometry and inlet conditions were varied to appraise model utility and sensitivity to flow conditions. TF-41 engine test data were used to establish engine exhaust static temperature and velocity. Static pressure at the engine exit was fixed at atmospheric pressure ($2116.0 \text{ lb}_f/\text{ft}^2$) for this study. Engine exit velocity was found by computing ρ from the equation of state for a perfect gas and using the one-dimensional mass conservation equation.

$$\rho = \frac{P}{RT}$$

and

$$V_{\text{engine}} = \frac{\dot{m}_{\text{engine}}}{\rho A_{\text{engine}}}$$

where \dot{m} = total mass flow through engine
(including bypass air)

A = area of exhaust plane

Engine exit static temperature was computed using the turbine outlet temperature and the bypass ratio given in Reference 7. A summary of these parameters is shown in Table II.

TABLE II
TF-41 TEST CONDITIONS

Power Setting	\dot{m} (lb _m /sec)	T _{exit} (°R)	V _{exit} (ft/sec)	Exit Mach Number
Idle	100	800	594	0.43
80%	150	900		
90%	200	927	1376	0.92
94%	238	955		
97%	249	970		
100%	263	1001		

A specific flow condition was chosen to provide a solution to which all succeeding solutions could be compared. That condition was: idle engine power setting with an augmentation ratio (AR) of 0.5. The geometry was fixed as shown in Figure 3.

The "reference" flow condition was chosen as it provided low subsonic flow conditions at the engine exhaust plane ($M = 0.43$) and the augmentation ratio was typical for actual test conditions.

Pressure calculations were made along the dashed lines shown in Figure 7. The lines show only approximate locations since grid spacing was often altered when geometry was varied.

Eight computer runs were made to examine the usefulness of the model. Each run was allowed approximately 2.5 hours (1400 iterations) to assure solution convergence although most runs achieved practical convergence prior to this time. A summary of the study follows in Table III.

TABLE III

FLOW CONDITIONS

1. Reference flow condition was established as discussed above: Idle Power, $AR = 0.5$, Figure 3a geometry.
2. Two runs were made varying the AR : Idle Power, $AR = 0.75$ and 1.0 , Figure 3a geometry.
3. Two runs were made to change the length of the augments duct lip: Idle Power, $AR = 0.5$, Figure 3b, geometries.
4. One run varied the engine to augments separation distance: Idle Power, $AR = 0.5$, Figure 3c, geometry.
5. One run varied the augments radius: Idle Power, $AR = 0.5$, Figure 3d, geometry.
6. One run changed the power setting of the engine: 90% power, $AR = 1.0$, Figure 3a geometry.

VI. RESULTS AND DISCUSSION

A. FLOW CONDITION 1 (Reference Condition)

Streamlines and static temperature contours are shown in Figures 8a and 8b, respectively. Pressure gradients along axial and radial grid lines (Figure 7) are graphically displayed in Figures 8c through 8f. Pressure contours along axial and radial grid lines are displayed in Figures 8g through 8i. Figure 8j presents the variation in augmenter pressure rise as a function of iteration number.

1. Streamlines/Temperature Contours

Axisymmetric flow solutions are obtained with this method.

Therefore, boundary conditions on stream function are determined from

$$\rho V_R = - (1/R) \partial \psi / \partial Z \quad \text{and} \quad \rho V_Z = (1/R) \partial \psi / \partial R$$

For example, the mass flow rate of a TF-41 engine is 100 lb_m/sec at idle power setting. Then, for uniform inlet velocity and density

$$\Delta \psi = \psi - \psi_o = \psi = \frac{\dot{m}}{2\pi} = \frac{100}{2\pi} = 15.9 \text{ lb}_m/\text{sec-radian}$$

as is shown in Figure 8a.

Two distinct regions of recirculation are apparent in Figure 8a. One prominent region exists above the augmenter tube bounded on two sides by the test cell ceiling and wall. Points of stagnation are shown located on the exterior augmenter tube surface and cell wall.

The second prominent region of recirculation is located downwind of the augmenter inlet lip. Close examination of the streamline having its origin at the lip reveals axial flow for a short distance followed by rapid directional change. Axial flow could have been the result of fixing the stream function at the first downwind corner as discussed in Section III.D.3.b.(3). However, an additional computer run was made with the same flow conditions except that the stream function at the downwind node was allowed to be computed normally. The solution for stream function was essentially identical to the first run. In any case, the lip has only small effects on the shape and size of the recirculation region. The recirculation region is formed at the low thrust, low augmentation ratio condition primarily by the radial component of the augmentation air as it flows into the augmenter.

The region of flow reattachment is well defined on the augmenter interior surface and is located approximately two augmenter diameters downstream of the inlet.

Temperature contours shown in Figure 8b are an indication of the amount of mixing occurring between engine flow and secondary air. From the non-dimensional mass fraction and temperature definitions, a thoroughly mixed flow would have a static temperature of 707 °R. Under these flow conditions, a well-mixed flow occurs approximately four augmenter diameters downstream of the augmenter inlet. The temperature contours

clearly show the effect of secondary air entrainment and recirculation within the augments tube on the temperature field.

2. Pressure Recovery

a. Axial (z-direction)

Pressure gradients along lines A-A through E-E (Figure 7) are shown in Figures 8c, d and e. Lines labeled A-A and B-B are axial lines having their origin at the engine exit plane and terminating one node upstream of the augments exit. Lines C-C, D-D and E-E extend between the third node in the axial direction and the node immediately upstream of the augments exit.

Large negative pressure gradients exist along all lines from the engine exit plane to just inside the augments inlet plane. Lines A-A and B-B exhibit the largest gradients in this region and examination of the solution reveals the exhaust jet rapidly departing from the uniform inlet velocity (plug flow) condition. Secondary air is being entrained in this area with line B-B being nearest the turbulent mixing zone of the exhaust jet. This may account for the largest pressure gradients existing along line B-B.

Pressure gradients along axial line F-F (Figure 7) are very small and are not shown. Static pressures along axial lines A-A through E-E are shown in Figures 8h and i. These pressure profiles are all initialized at $2116.0 \text{ lb}_f/\text{ft}^2$.

b. Radial (R-direction)

Pressure gradients and static pressures along G-F are shown in Figures 8f and 8g, respectively. The engine exhaust jet turbulent mixing zone is clearly indicated by fluctuating pressure gradients (Figure 8f). Static pressure is seen to increase toward the engine exhaust jet centerline which is due primarily to the secondary air momentum in the negative R-direction.

No appreciable pressure gradients existed along radial line H-H which is located downstream of the flow reattachment point.

c. Total Axial Static Pressure Rise

Total rise (ΔP) was defined as the static pressure difference between end-points of the lines discussed above. ΔP is plotted against number of iterations in Figure 8j. The upwind end pressure for all lines is reference pressure but each line is seen to exhibit a unique value for ΔP at 1400 iterations. No pressure gradients exist in the radial direction downwind of the reattachment point. Therefore, ΔP values should be identical in magnitude for lines A-A through E-E when the solution is converged.

Close examination of the pressure gradients (Figures 8c through 8e) reveals line E-E to have small, "well behaved" gradients compared with lines A-A through D-D. Figure 8j indicates that the ΔP calculation for line E-E "converged" relatively early (1000 iterations). For these reasons, pressure rise was taken to be that computed for E-E ($47 \text{ lb}_f/\text{ft}^2$).

The differences in the pressure rise calculated along axial grid lines can be due to several things. The number of iterations has a dominant effect on the calculated pressure rise. The dependent variables (ω , ψ , K , ϵ , T) vary only slightly with increased iteration time. However, the pressure calculation is apparently very sensitive to small changes in the stream function and density. This is probably because $\frac{\partial p}{\partial z}$ is a function of second derivatives of ψ . In addition, pressure rise is calculated by assuming linear variations in gradient between grid points and pressure has been held fixed for purposes of calculating the density (i.e., $\rho = \rho(T)$). Improved accuracy might be obtained if pressure was calculated periodically in the solution in order that pressure effects on density may be taken into account. It was found that finer grid spacing did not appreciably affect the pressure calculation. Another possible error source may enter through the use of upwind differences and/or the inadequacy of the Jones-Launder model for the flow geometry under investigation. However, checks on the solution indicated that mass was conserved at each axial location with less than 14 percent error.

B. FLOW CONDITION 2

Augmentation ratio (AR) was varied with idle power setting to assess the effect on total static pressure rise through the system. Solution convergence and pressure gradients were similar to Flow Condition 1 and axial line E-E was again

chosen to determine the value of ΔP . The solutions along the other axial lines had approximately the same slope on an AR vs. ΔP plot but were different in magnitude as discussed above.

Figure 9a shows decreasing ΔP with increased AR. This result qualitatively correlates with Bailey [8,9] who experimentally varied exit pressure on a small jet pump and determined secondary mass entrainment. As the augmentation air is increased for a fixed engine flow there is less momentum differential between the two streams. This apparently causes the decreased pressure rise with increased AR. In actual test cell operation there is a unique AR for each engine flow rate (assuming the augments is fixed in design and position). The actual value is determined from the pressure rise in the augments tube being equal to the pressure losses through the rest of the test cell. If pressure losses through the inlet and exit stacks (with their associated acoustic and pollution abatement equipment) and through the horizontal portion of the cell can be estimated as a function of flow velocity, then the AR can be found in an iterative manner by using the ΔP vs. AR plot determined with the model for a particular augments design and position.

Figures 9b and 9c show the effect of AR on the stream function and temperature distributions, respectively. As the AR is increased the axial velocity component of the secondary air dominates over the radial component. The latter

component was observed above to be the major cause of the recirculation region. Thus, as the AR is increased, the recirculation region within the augments is seen to decrease in size and mixing occurs more rapidly.

C. FLOW CONDITION 3

The augments duct lip length was varied by 0.63 ft (2.1 ft to 2.73 ft augments inlet radius). Stream function and temperature fields are shown in Figures 10a through 10d. No appreciable change in calculated pressure rise was observed. This result apparently occurs because at low augmentation ratios the size of the inlet lip has very little effect on the size of the recirculation region within the augments. A greater effect of duct lip length on pressure rise could be expected at higher augmentation ratios.

D. FLOW CONDITION 4

Engine to augments inlet separation was increased to 2.5 ft (from 1.5 ft). Stream function and temperature contours are included as Figures 11a and 11b. No appreciable change in pressure rise was noted along axial grid line E-E when compared with Flow Condition 1.

The stream function solution indicated that no appreciable change occurred within the augments when the distance was increased. Again, a more significant effect could be expected for higher augmentation ratios. Moving the augments closer to the engine should have a major effect on the recirculation

region and the calculated pressure rise. As discussed above, the inlet velocity profile for the augmentation air was assumed to increase linearly from the cell ceiling to the engine at a location just upstream of the engine exhaust. This profile would change as the augments position is changed. Since test cells are designed to provide uniform flow at the engine inlet, future investigations with the model should be made with the secondary air inlet specified as uniform at the engine inlet plane. In this case, the velocity profile near the engine exhaust plane would be free to develop in a realistic manner.

E. FLOW CONDITION 5

Augments radius was increased by 0.5 ft to 3.5 ft while keeping the duct inlet diameter fixed. Figures 12a and 12b present the temperature and stream function contours. Pressure rise (ΔP) along E-E was diminished to $37 \text{ lb}_f/\text{ft}^2$ from the reference condition value of $47 \text{ lb}_f/\text{ft}^2$. Although only one run was made, this pressure loss is considerable and indicates ΔP decreases with increasing augments diameter (given fixed inlet flow conditions). The increased size of the recirculation region (which consists primarily of augmentation air) may contribute to this pressure loss.

F. FLOW CONDITION 6

Engine power setting was increased to 90% and the A R was set at 1.0 which is typical for an actual engine test. Figure 13a shows the recirculation region smaller with flow

reattachment farther upstream. The temperature contours (Figure 13b) show engine exhaust and secondary air being thoroughly mixed farther down the augmentor tube than occurred at idle flow.

Pressure rise versus number of iterations is shown in Figure 13c. The numerical values of the dependent variables did not change appreciably after 1400 iterations. However, ΔP 's differed in value considerably along lines A-A through E-E, so no definitive pressure rise could be derived from the results. The solution procedure (which assumes incompressible flow and uses the associated elliptic equations) used in this study is questionable when applied at the higher subsonic Mach numbers.

VII. CONCLUSIONS AND RECOMMENDATIONS

A. CONCLUSIONS

The model provides axisymmetric flow visualizations in turbojet test cells and augments tubes for low subsonic flow conditions. These can be used to identify regions of recirculation and to assess the amount of mixing occurring between engine exhaust gases and secondary air. Optimum locations for pollution sampling equipment can be selected by examining the numerical solutions.

Static pressure rise within the augment tube can be calculated for a given flow condition and augment design from converged solutions, provided that regions of "steep" gradients in variables are avoided. Total pressure rise through the system can be found and factors which influence this rise (augment design and location, engine flow rate, test cell size, and etc.) can be studied.

High subsonic flows invalidate the use of partial differential equations of the elliptic type; therefore, the model provides realistic solutions only at low subsonic Mach numbers.

B. RECOMMENDATIONS

1. Additional computer runs should be made to firmly establish the effects of augment and cell geometry on flow mixing and pressure rise (ΔP). For example, the effects of moving the augment inlet closer to the engine exit plane

and moving the test cell wall forward to the augments inlet plane should be considered. In addition, the program could also be easily modified to extend the augments duct lip in the opposite direction.

2. The cell "inlet" position should be moved upstream to the engine inlet plane by the addition of a few grid lines in the z-direction. Plug flow could be assumed at the "new" cell inlet and the resultant flow field would show the actual velocity distribution at the "cell inlet" used in this study. In addition, this would permit calculation of exhaust gas recirculation.

3. Static pressure and velocity measurements should be taken under various test conditions at NARF Alameda. The size and shape of the recirculation region located above the augments should be qualitatively verified by photographing a tufted grid placed between the test cell augments tube and ceiling. These data would help in validation/improvement of the computer model.

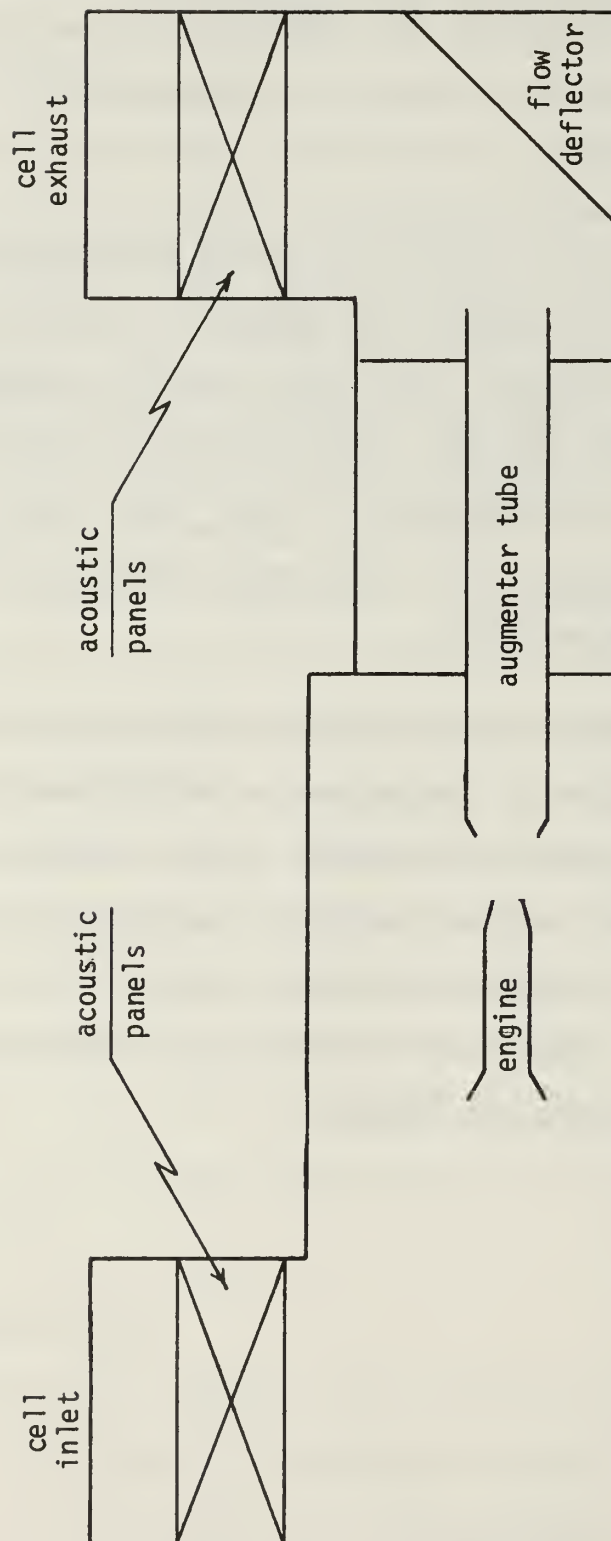


FIGURE 1. TEST CELL GEOMETRY

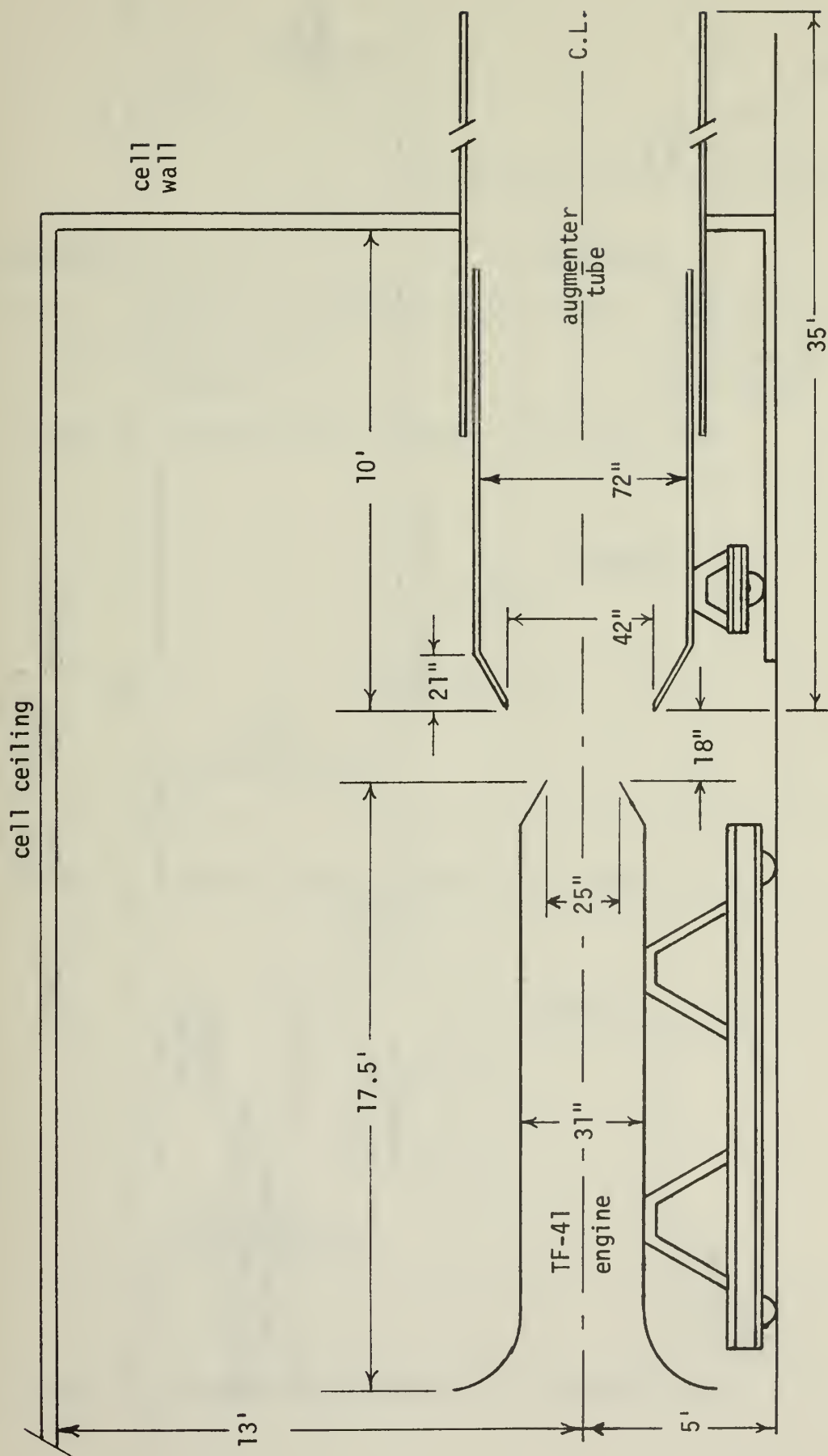


FIGURE 2. TF-41 TEST CONFIGURATION



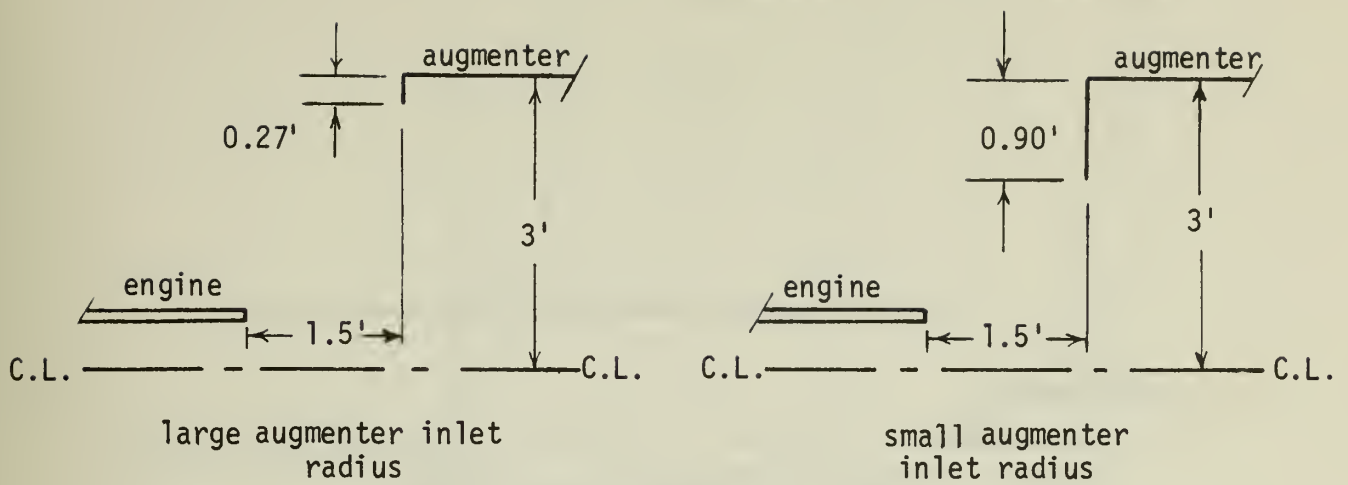


FIGURE 3b. COMPUTER MODEL GEOMETRY: FLOW CONDITION 3

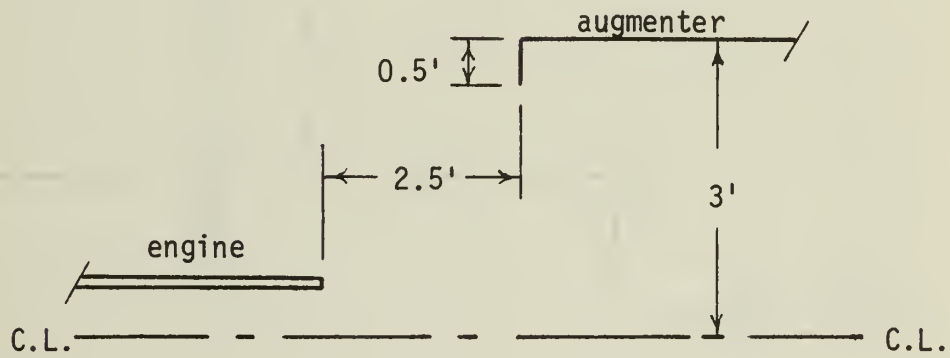


FIGURE 3c. COMPUTER MODEL GEOMETRY: FLOW CONDITION 4

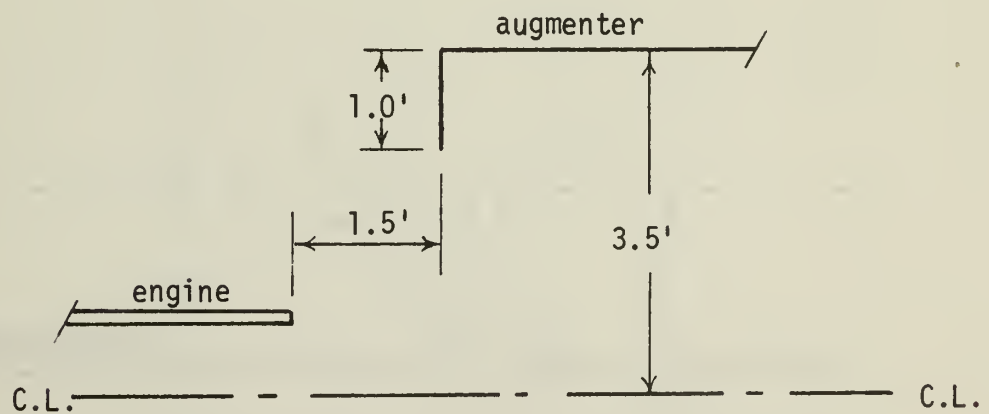


FIGURE 3d. COMPUTER MODEL GEOMETRY: FLOW CONDITION 5

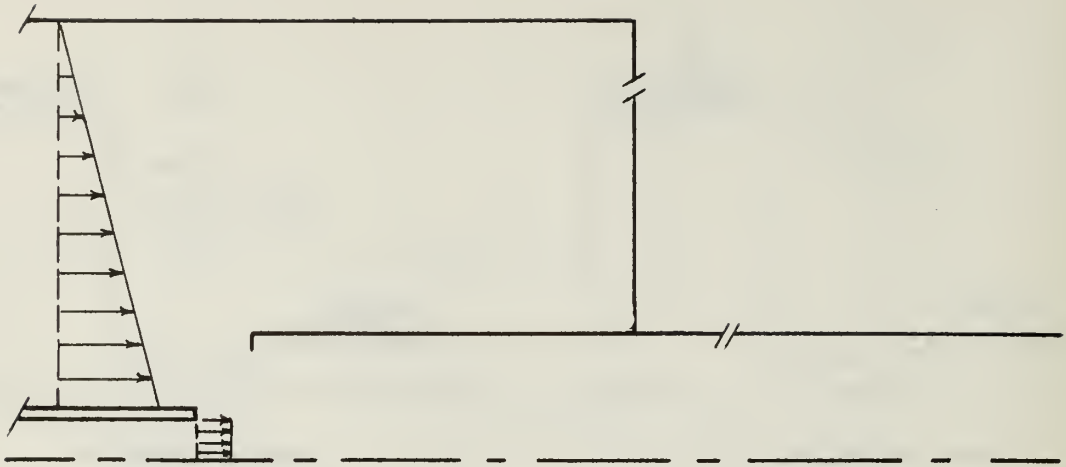


FIGURE 4. VELOCITY PROFILES IN INLET FLOWS

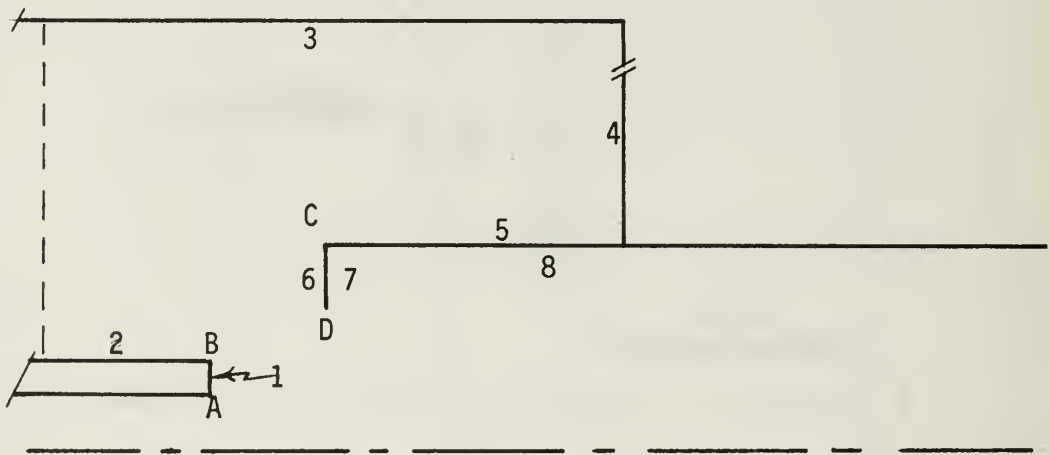


FIGURE 5. IDENTIFICATION OF BOUNDARIES

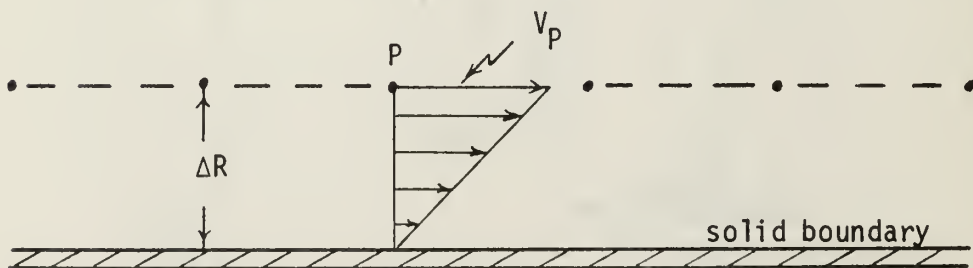


FIGURE 6. LAMINAR SUBLAYER VELOCITY PROFILE

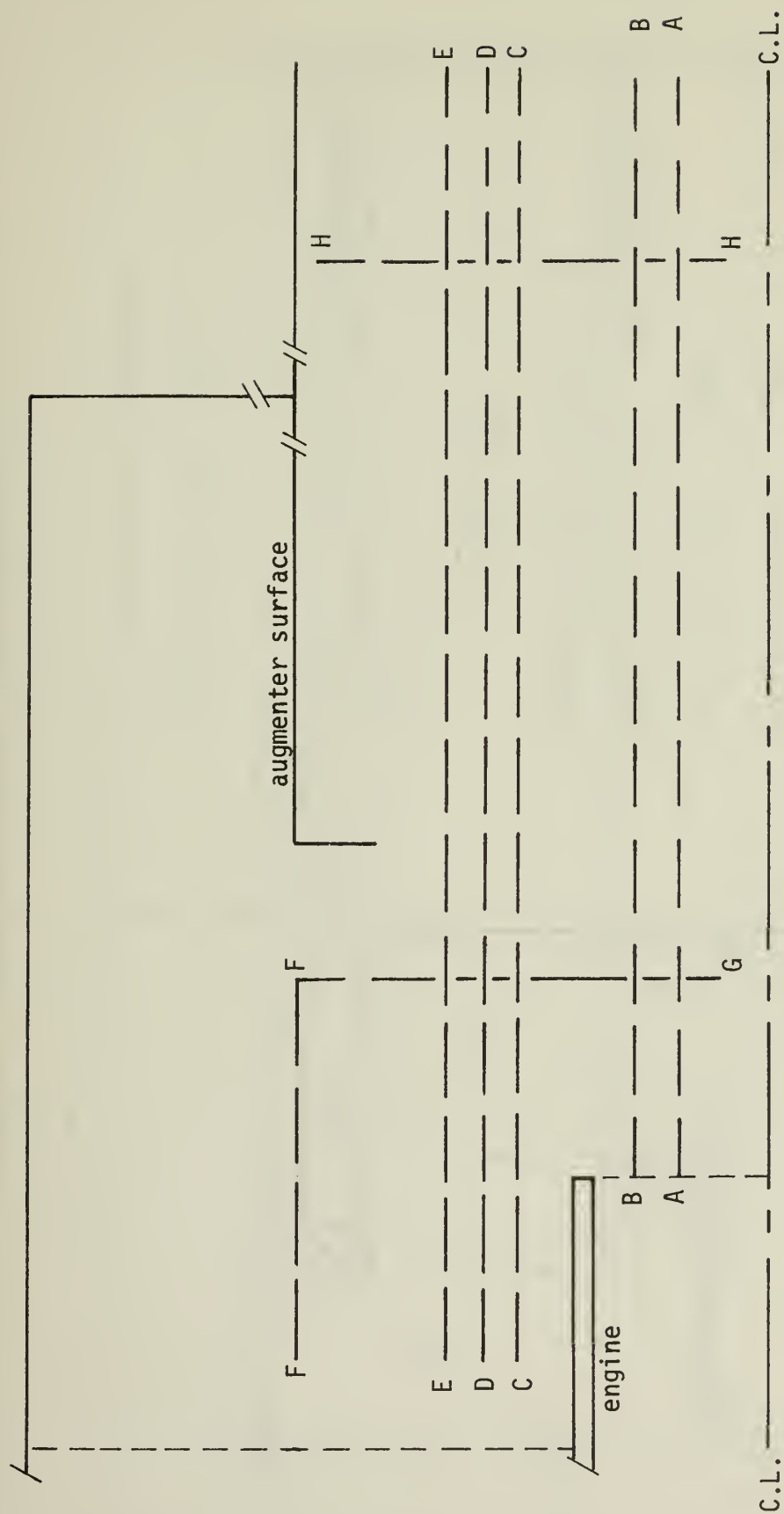


FIGURE 7. LOCATION OF GRID LINES FOR PRESSURE CALCULATIONS

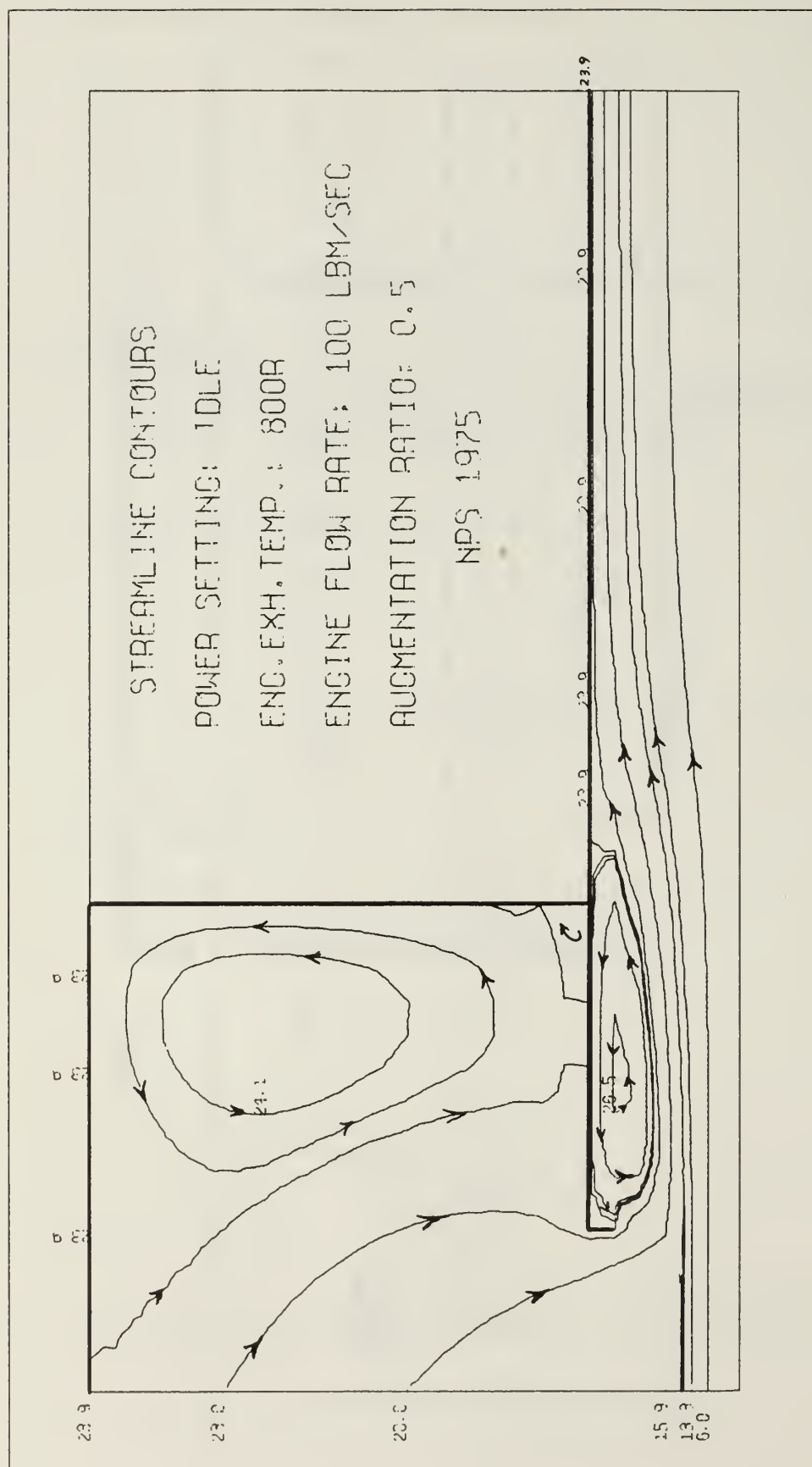


FIGURE 8a. STREAMLINE CONTOURS: FLOW CONDITION 1

TEMPERATURE CONTOURS

POWER SETTING: IDLE

ENG. EXH. TEMP.: 800R

ENGINE FLOW RATE: 100 LBM/SEC

AUGMENTATION RATIO: 0.5

NPS 1975

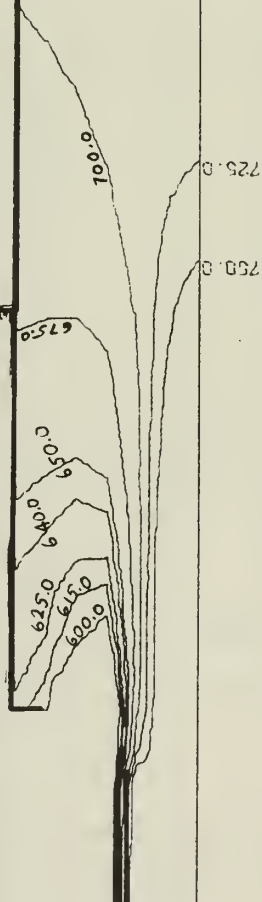


FIGURE 8b. TEMPERATURE CONTOURS: FLOW CONDITION 1

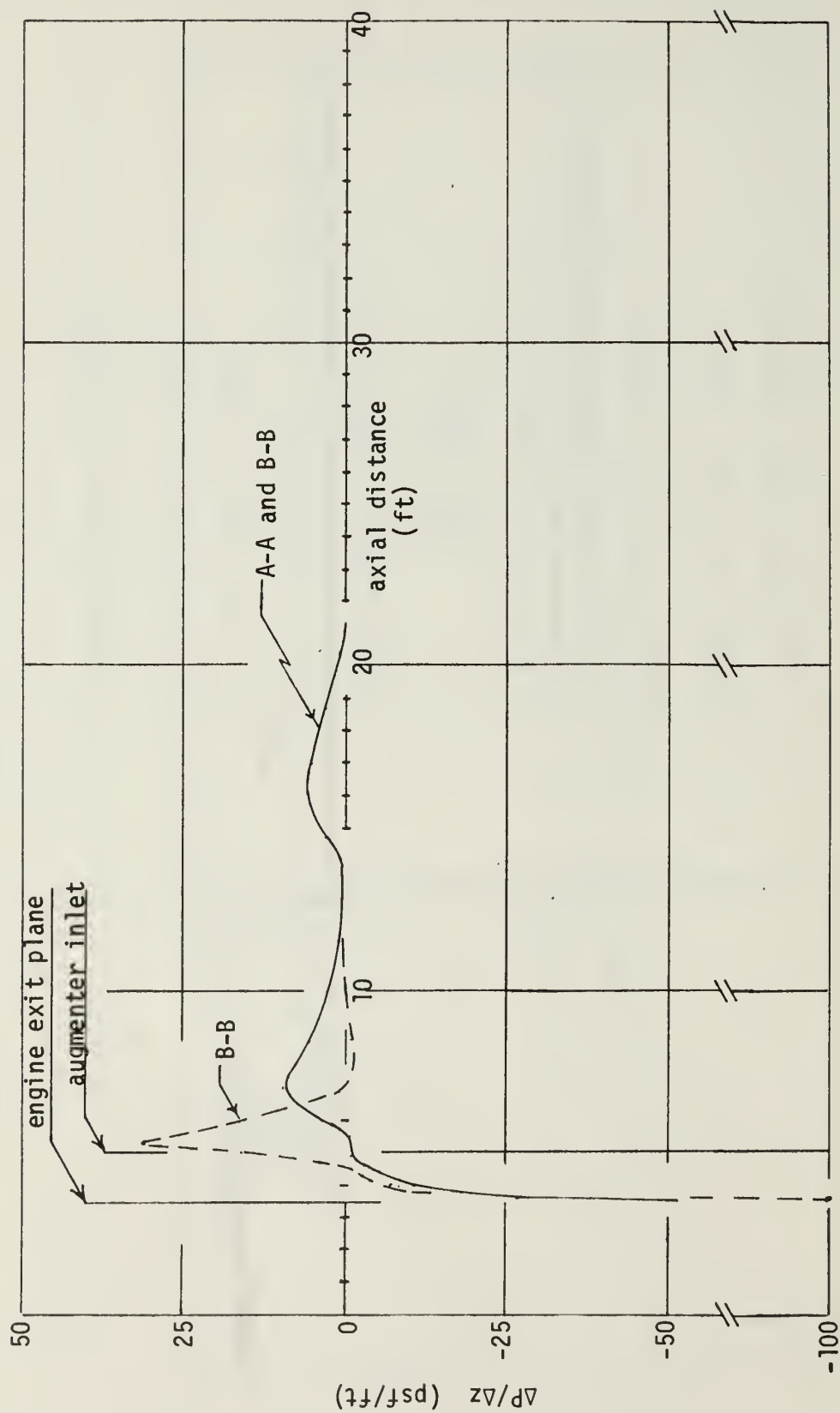


FIGURE 8c. AXIAL PRESSURE GRADIENTS: FLOW CONDITION 1
(LINES A-A AND B-B)

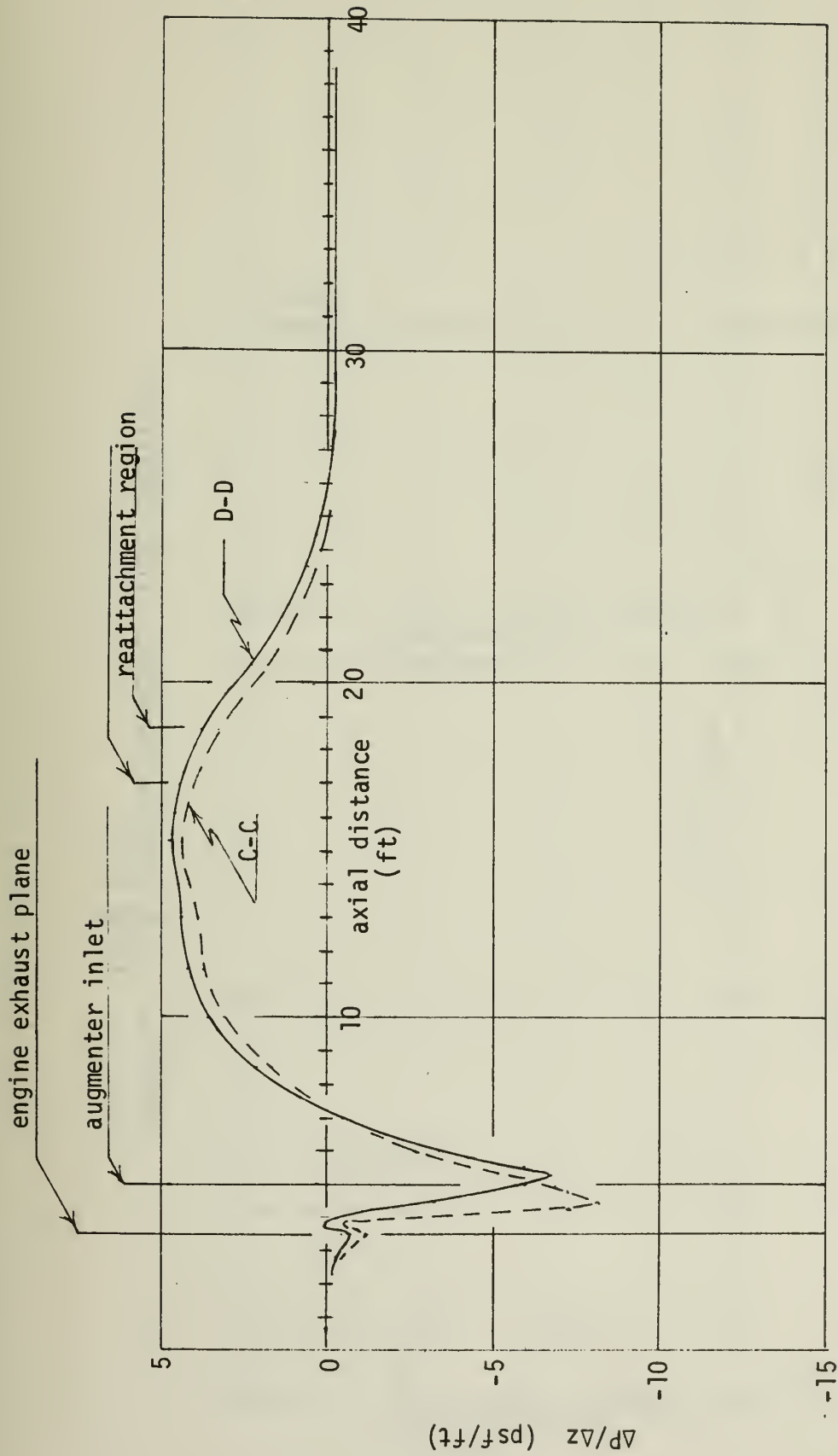


FIGURE 8d. AXIAL PRESSURE GRADIENTS: FLOW CONDITION 1
(LINES C-C AND D-D)

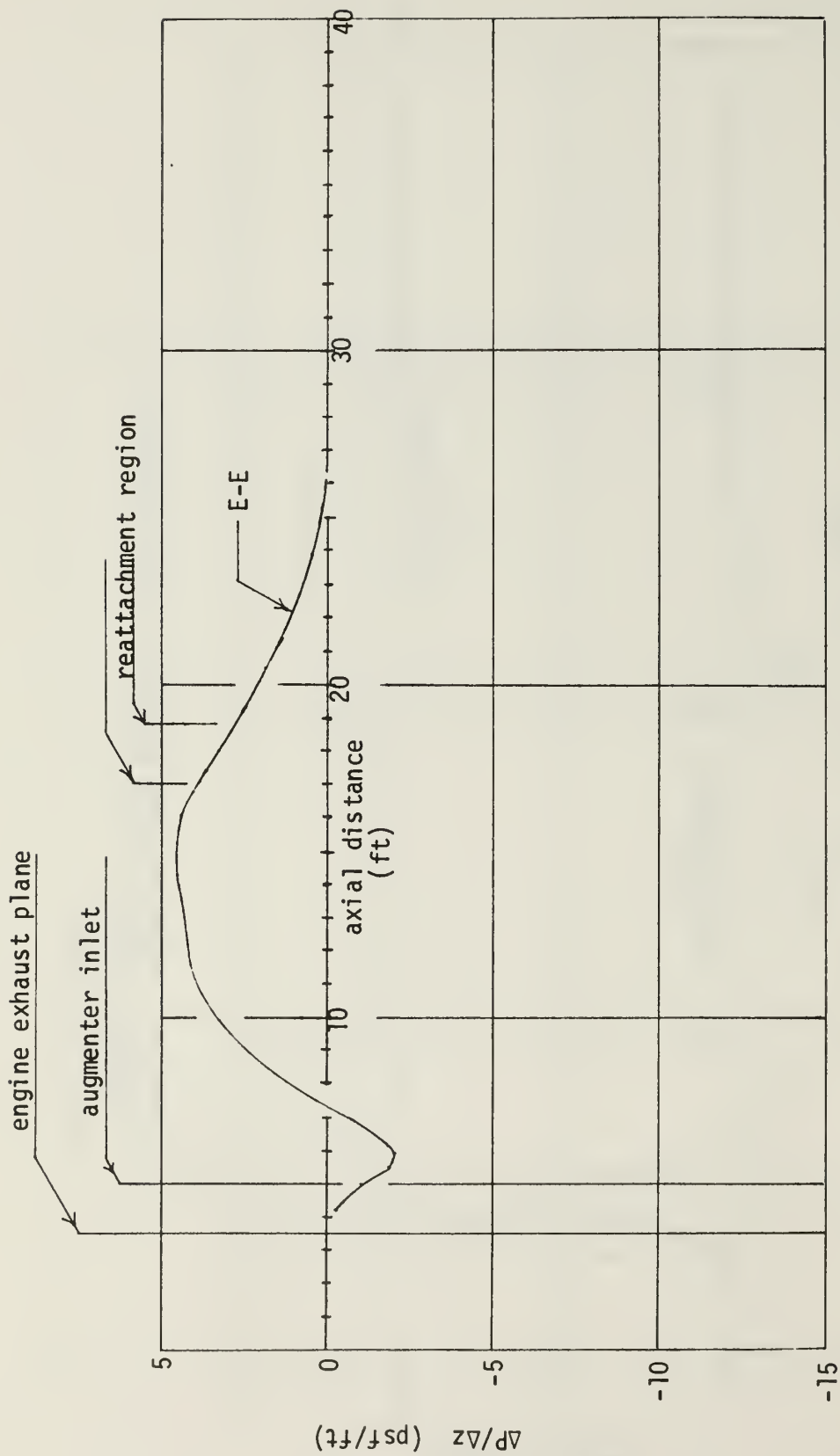


FIGURE 8e. AXIAL PRESSURE GRADIENTS: FLOW CONDITION 1
(LINE E-E)

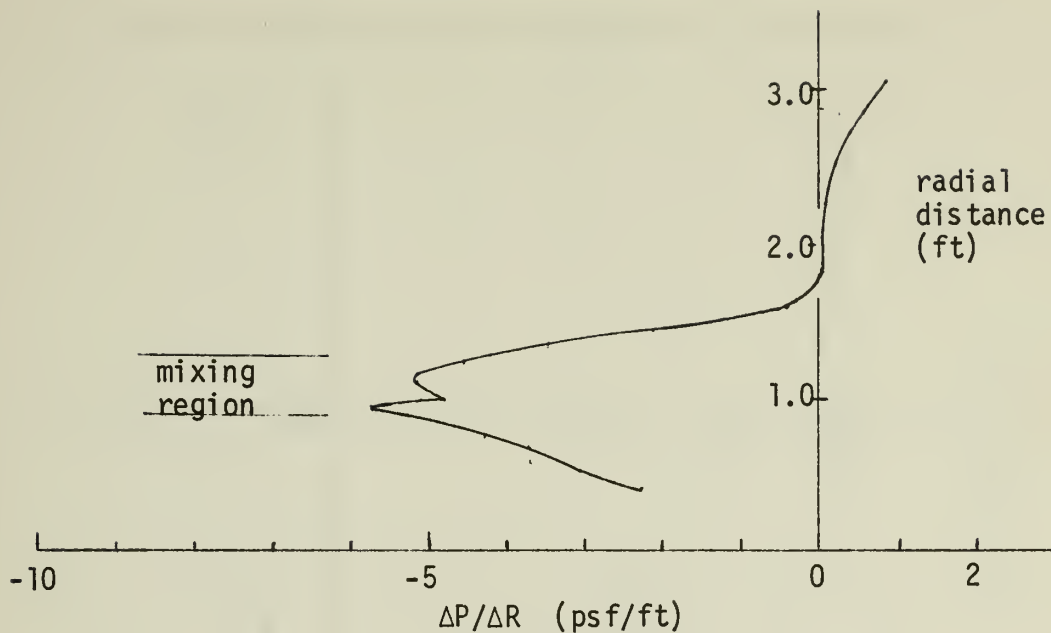


FIGURE 8f. RADIAL PRESSURE GRADIENTS:
FLOW CONDITION 1
(LINE G-H)

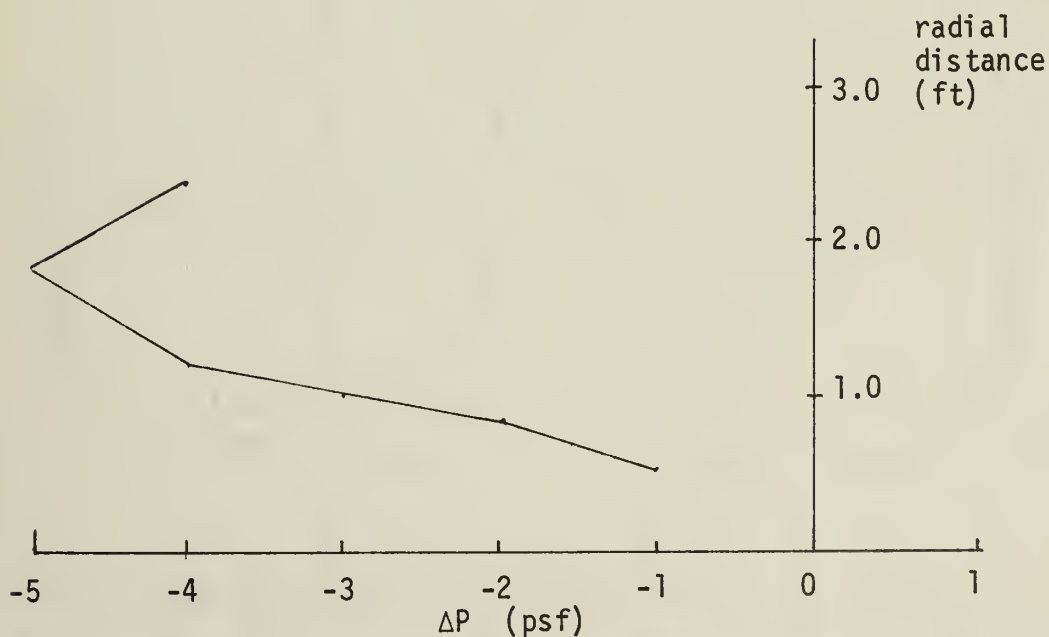


FIGURE 8g. RADIAL STATIC PRESSURE VARIATIONS:
FLOW CONDITION 1
(LINE G-H)

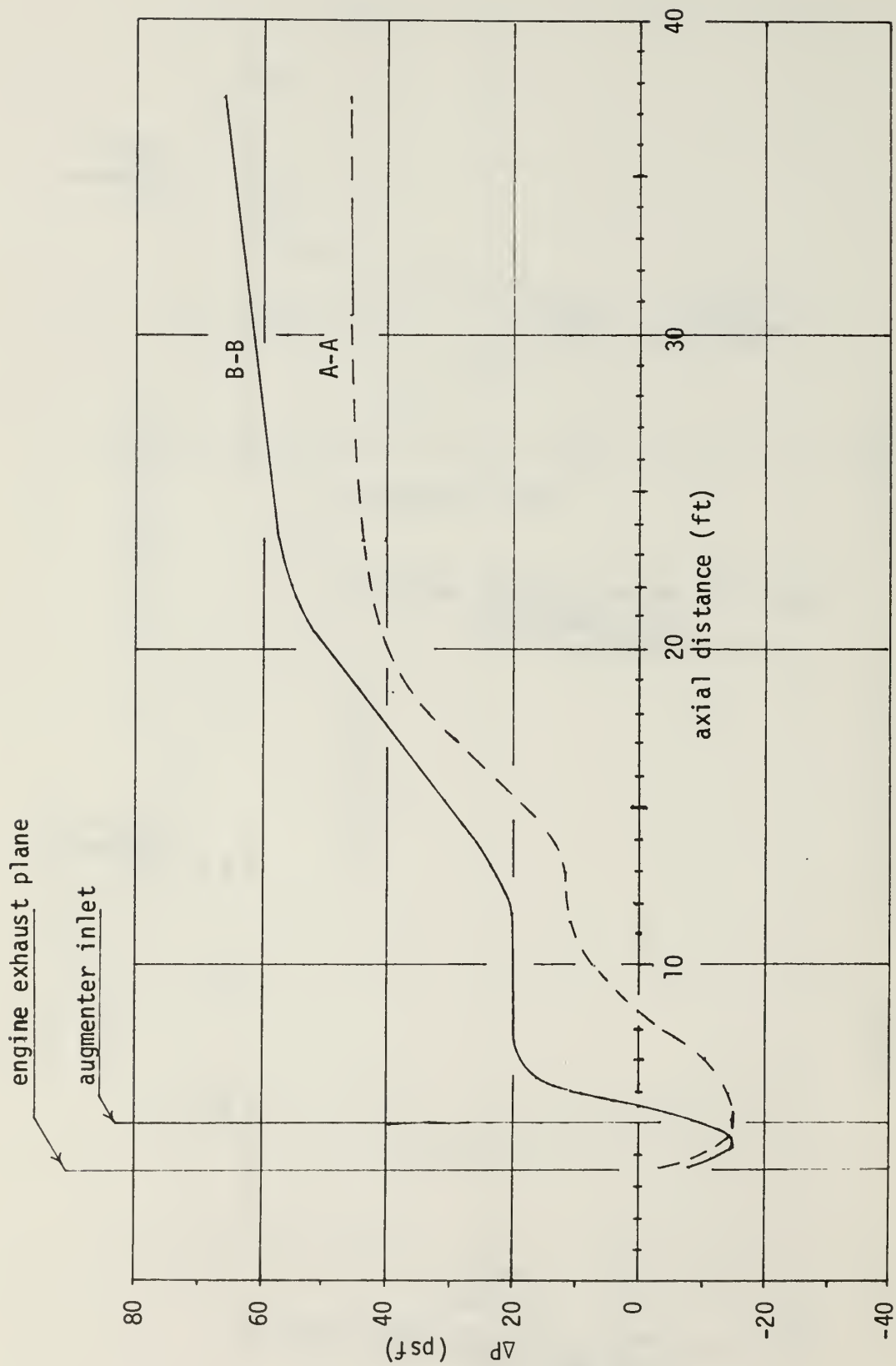


FIGURE 8h. AXIAL STATIC PRESSURE VARIATIONS:
FLOW CONDITION 1
(LINES A-A AND B-B)

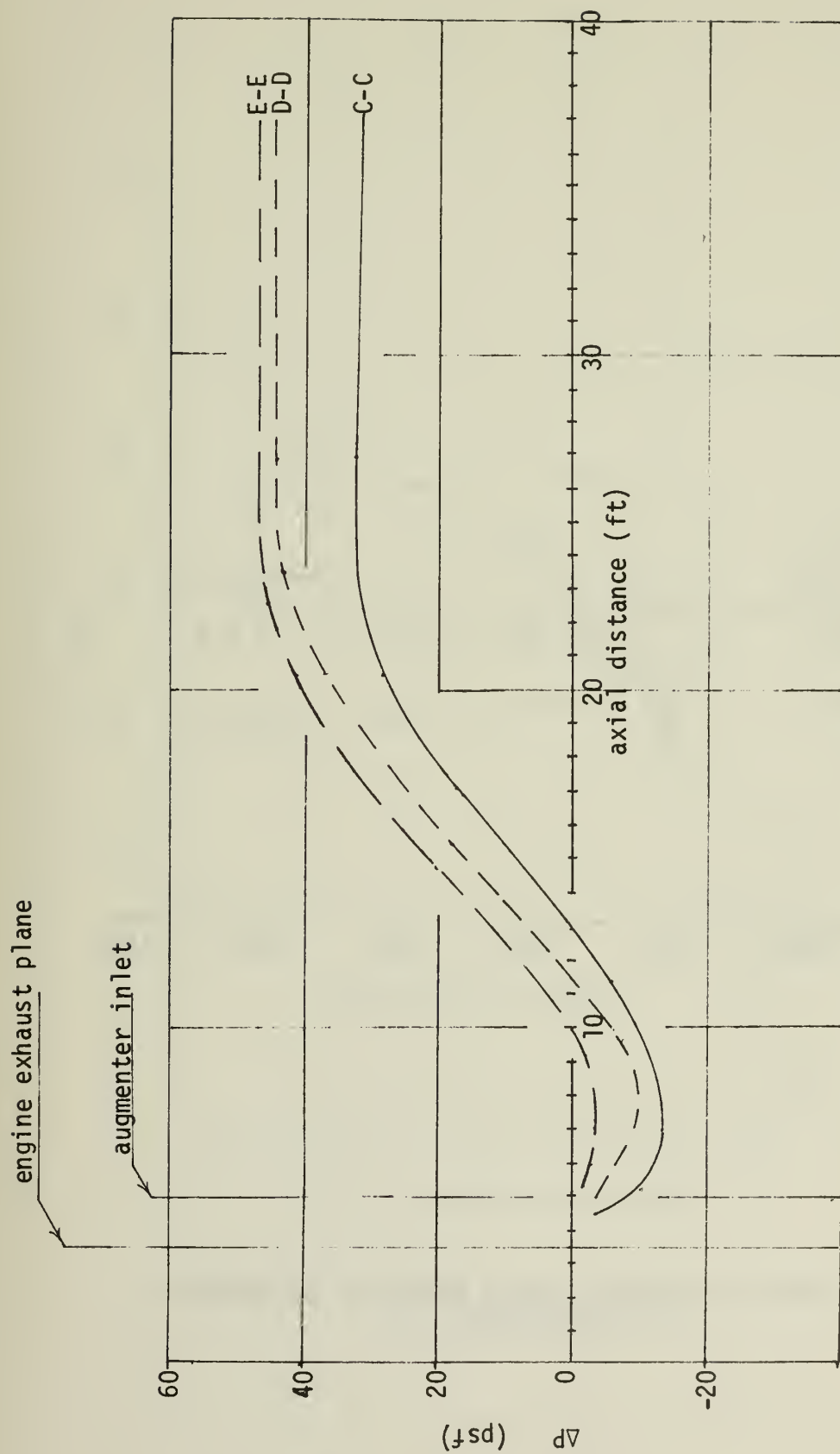


FIGURE 8i. AXIAL STATIC PRESSURE VARIATIONS: FLOW CONDITION 1
(LINES C-C THROUGH E-E)

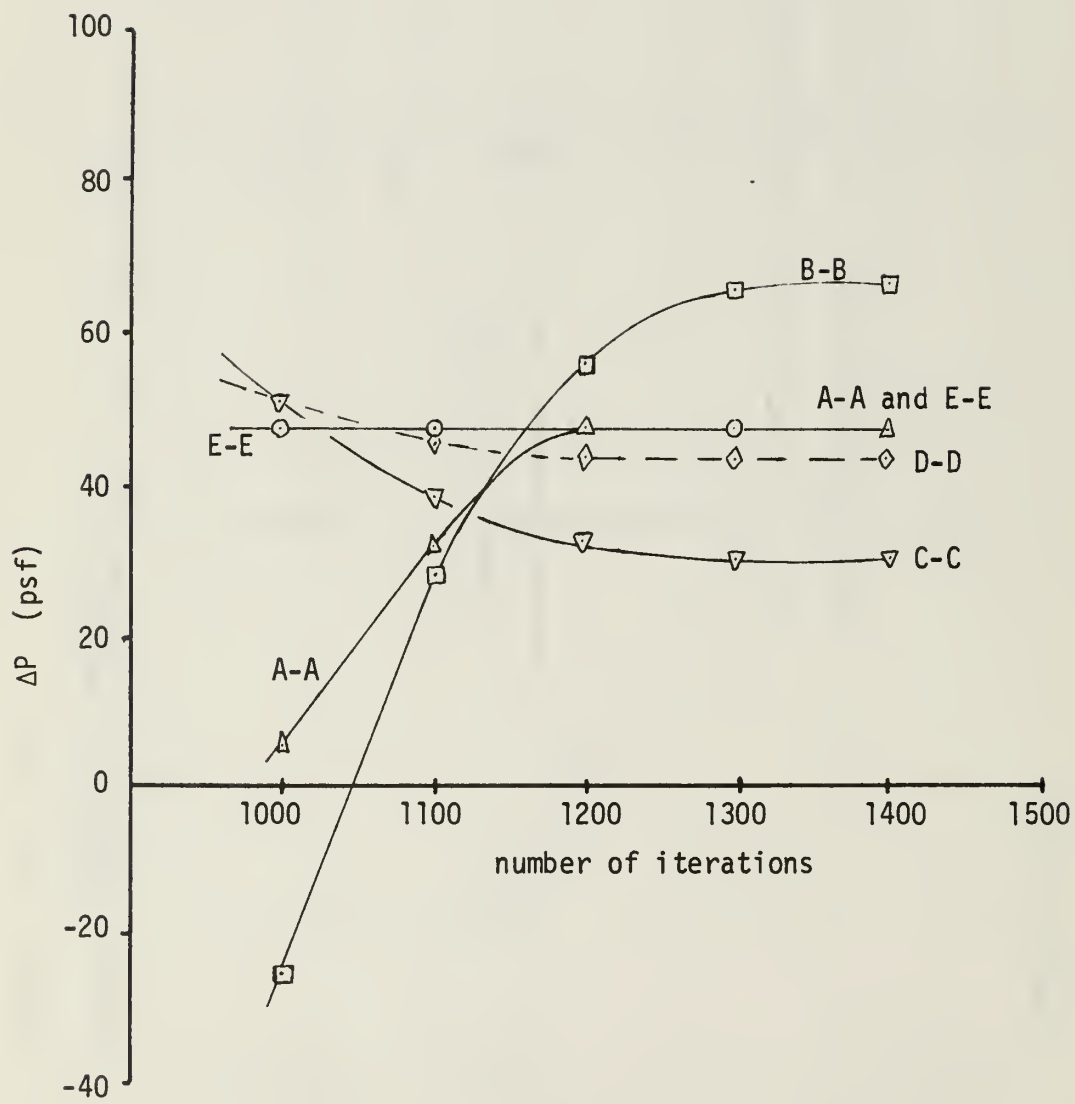


FIGURE 8j. ΔP RISE VERSUS NUMBER OF ITERATIONS:
FLOW CONDITION 1

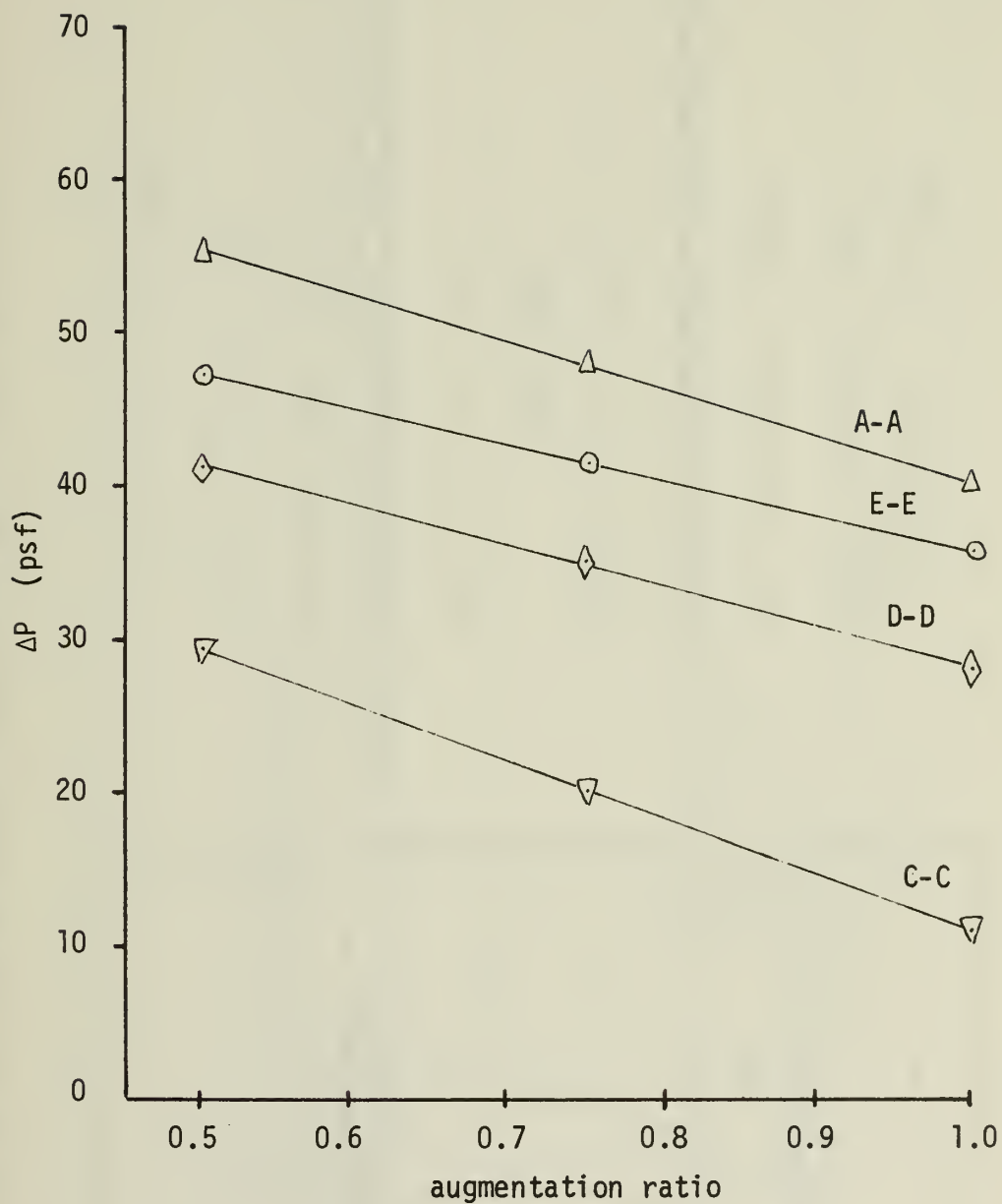


FIGURE 9a. ΔP RISE VERSUS AUGMENTATION RATIO:
FLOW CONDITION 1

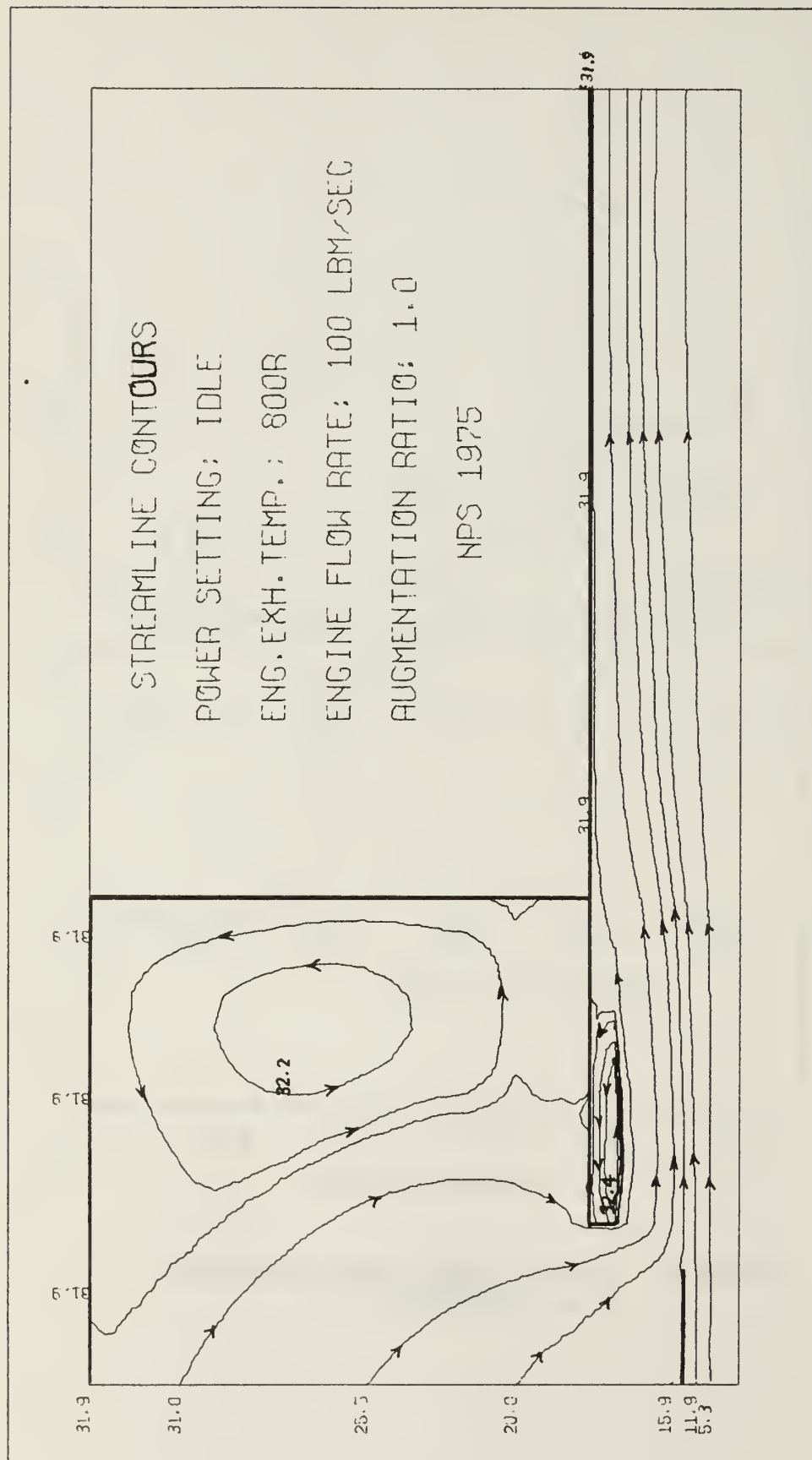


FIGURE 9b. STREAMLINE CONTOURS: FLOW CONDITION 2 (AR = 1.0)

TEMPERATURE CONTOURS

POWER SETTING: IDLE

ENG. EXH. TEMP.: 300R

ENGINE FLOW RATE: 100 LBM/SEC

AUGMENTATION RATIO: 1.0

NPS 1975

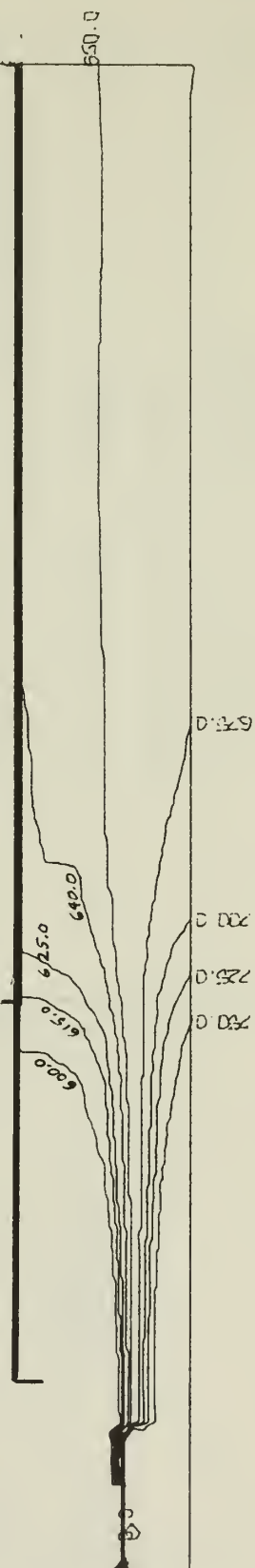


FIGURE 9c. TEMPERATURE CONTOURS: FLOW CONDITION 2 (AR = 1.0)

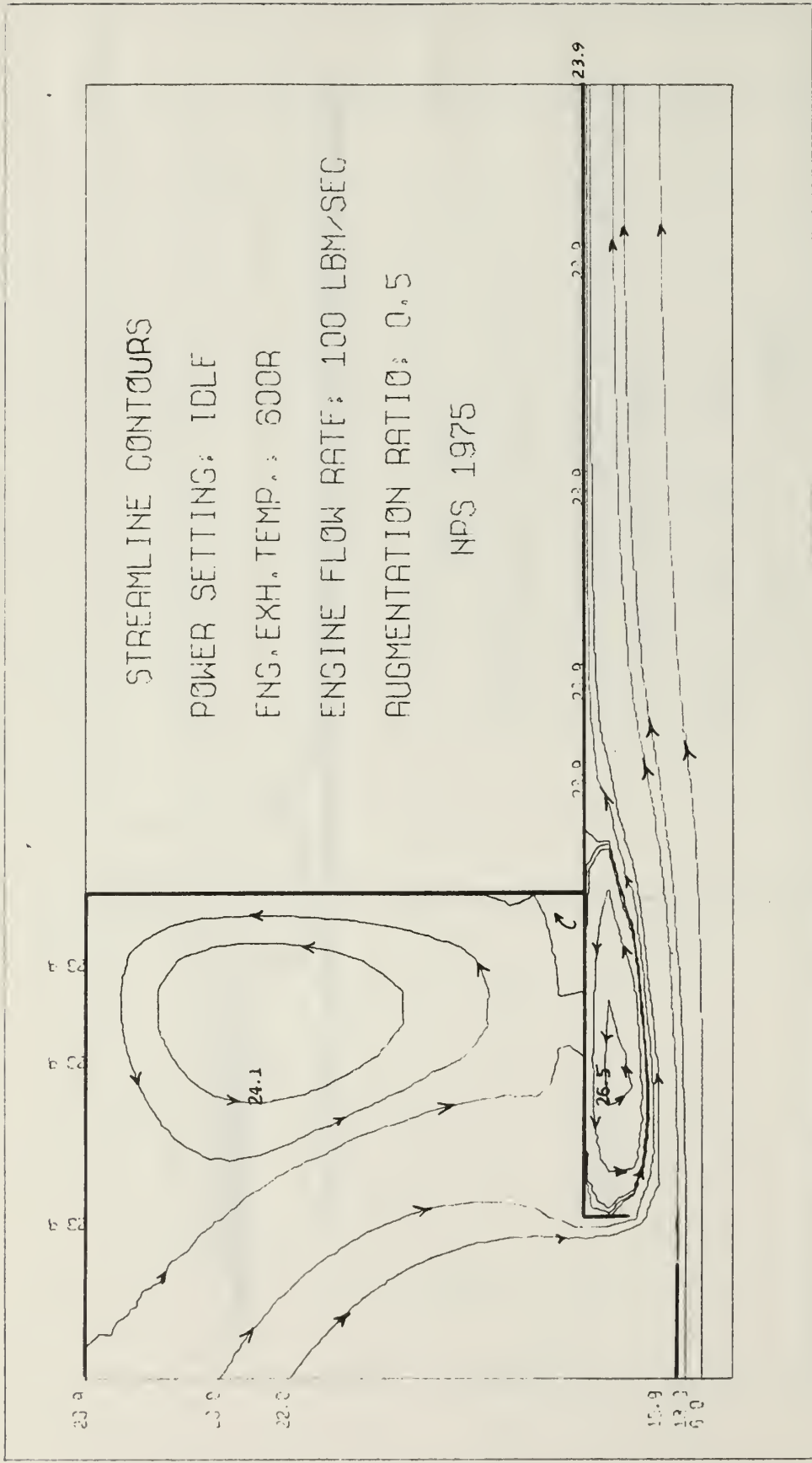


FIGURE 10a. STREAMLINE CONTOURS: FLOW CONDITION 3
(SMALL AUGMENTER INLET RADIUS)

TEMPERATURE CONTOURS

POWER SETTING: IDLE

ENG. EXH. TEMP.: 800R

ENGINE FLOW RATE: 100 LBM/SEC

AUGMENTATION RATIO: 0.5

NPS 1975

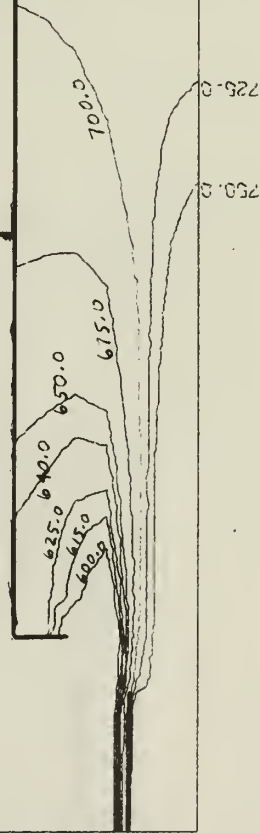


FIGURE 10b. TEMPERATURE CONTOURS: FLOW CONDITION 3
(SMALL AUGMENTER INLET RADIUS)

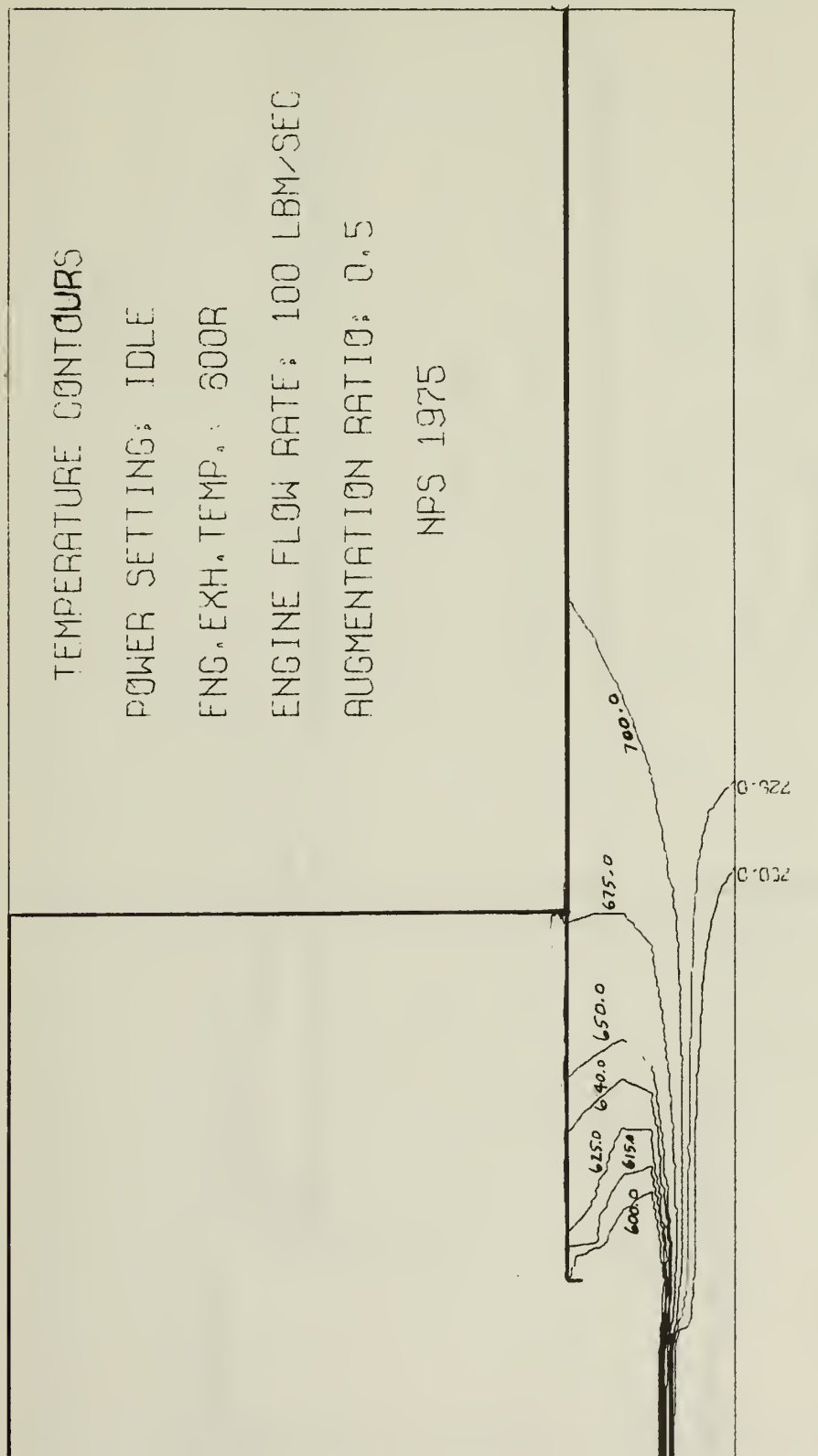


FIGURE 10d. TEMPERATURE CONTOURS: FLOW CONDITION 3
(LARGE AUGMENTER INLET RADIUS)

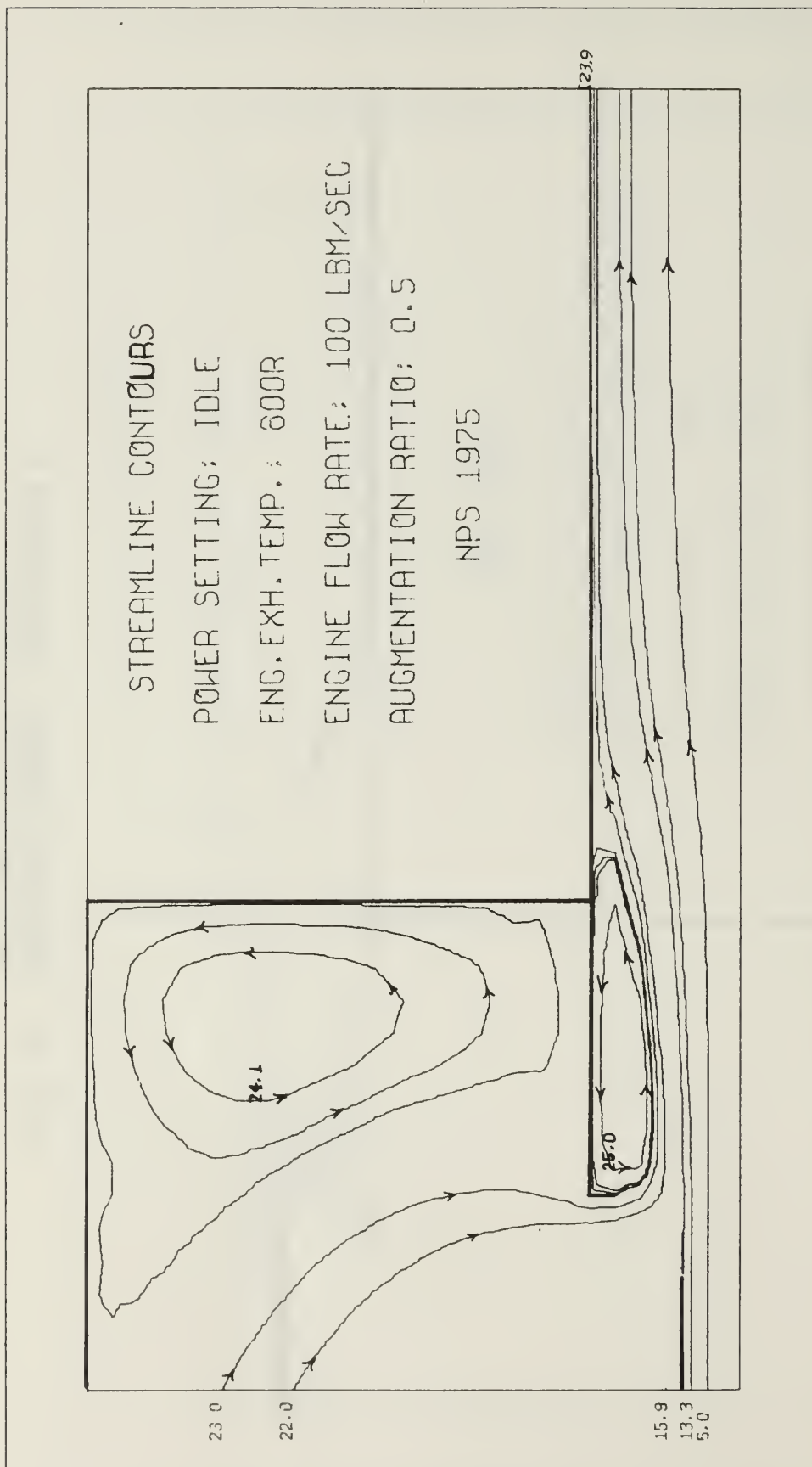


FIGURE 11a. STREAMLINE CONTOURS: FLOW CONDITION 4

TEMPERATURE CONTOURS

POWER SETTING: IDLE

ENG. EXH. TEMP.: 800R

ENGINE FLOW RATE: 100 LBM/SEC

AUGMENTATION RATIO: 0.5

NPS 1975

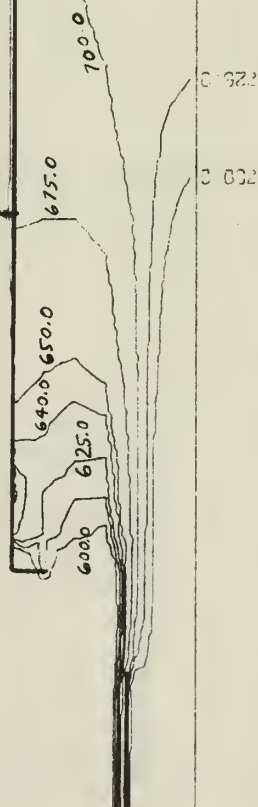


FIGURE 11b. TEMPERATURE CONTOURS: FLOW CONDITION 4

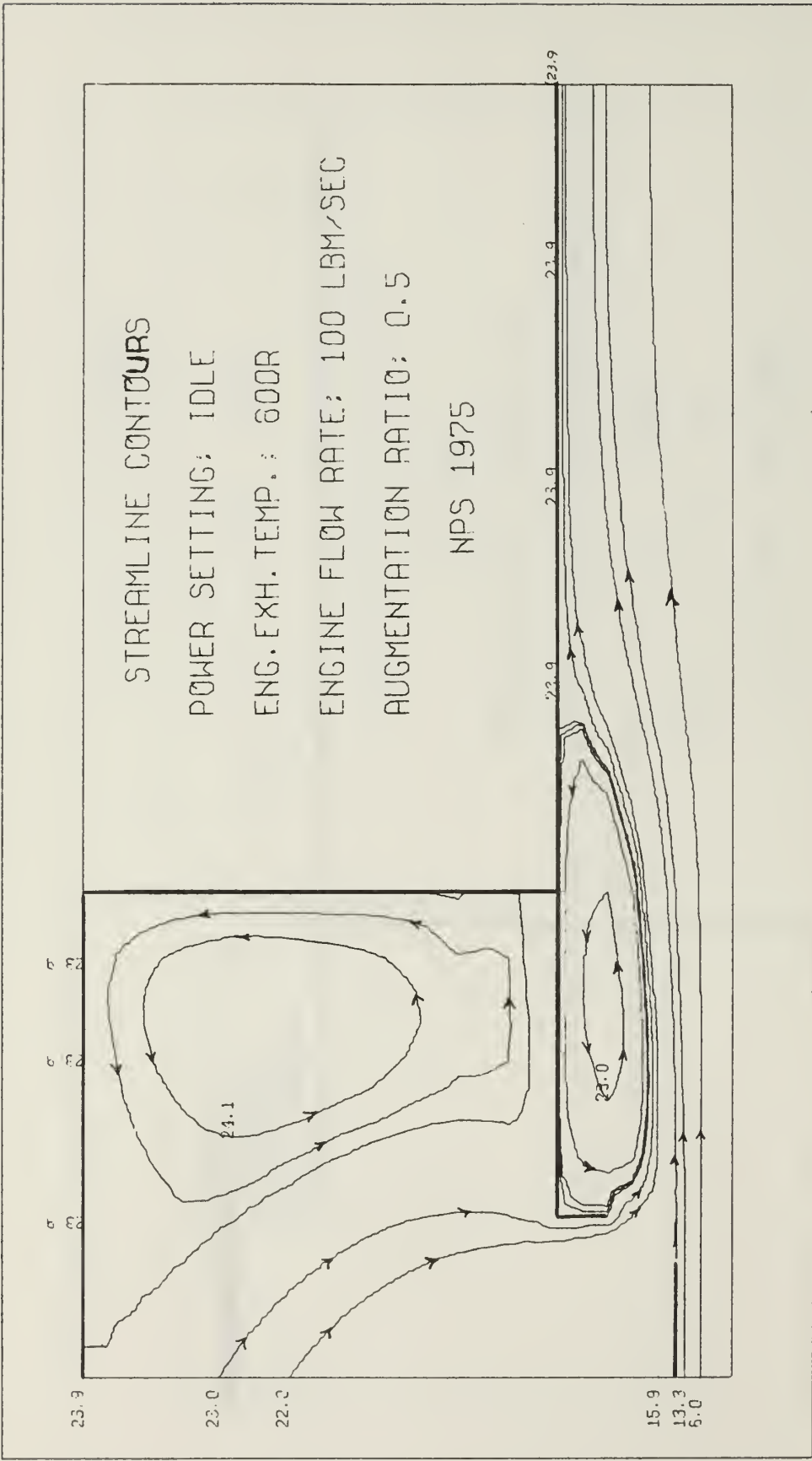


FIGURE 12a. STREAMLINE CONTOURS: FLOW CONDITION 5

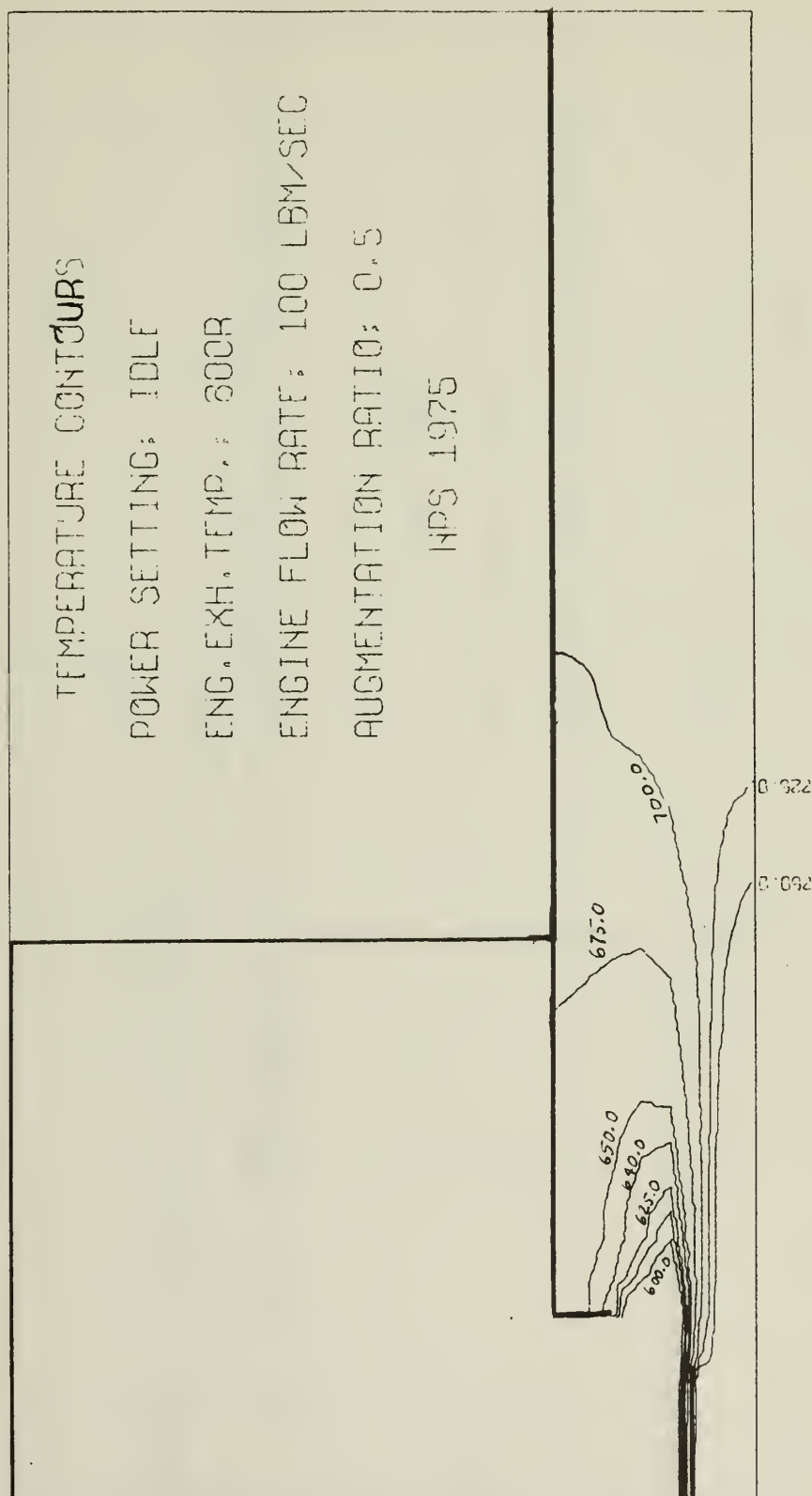


FIGURE 12b. TEMPERATURE CONTOURS: FLOW CONDITION 5

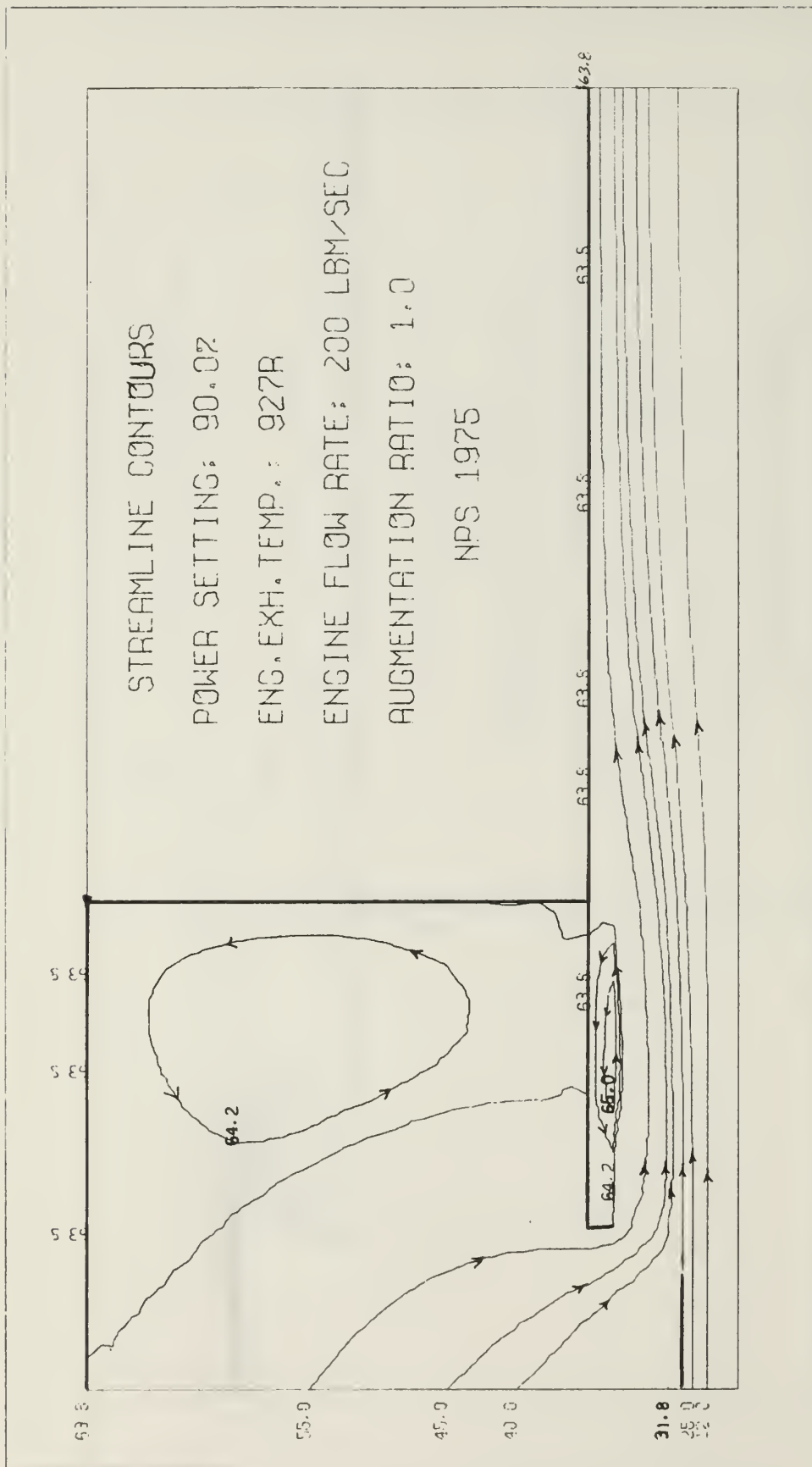


FIGURE 13a. STREAMLINE CONTOURS: FLOW CONDITION 6

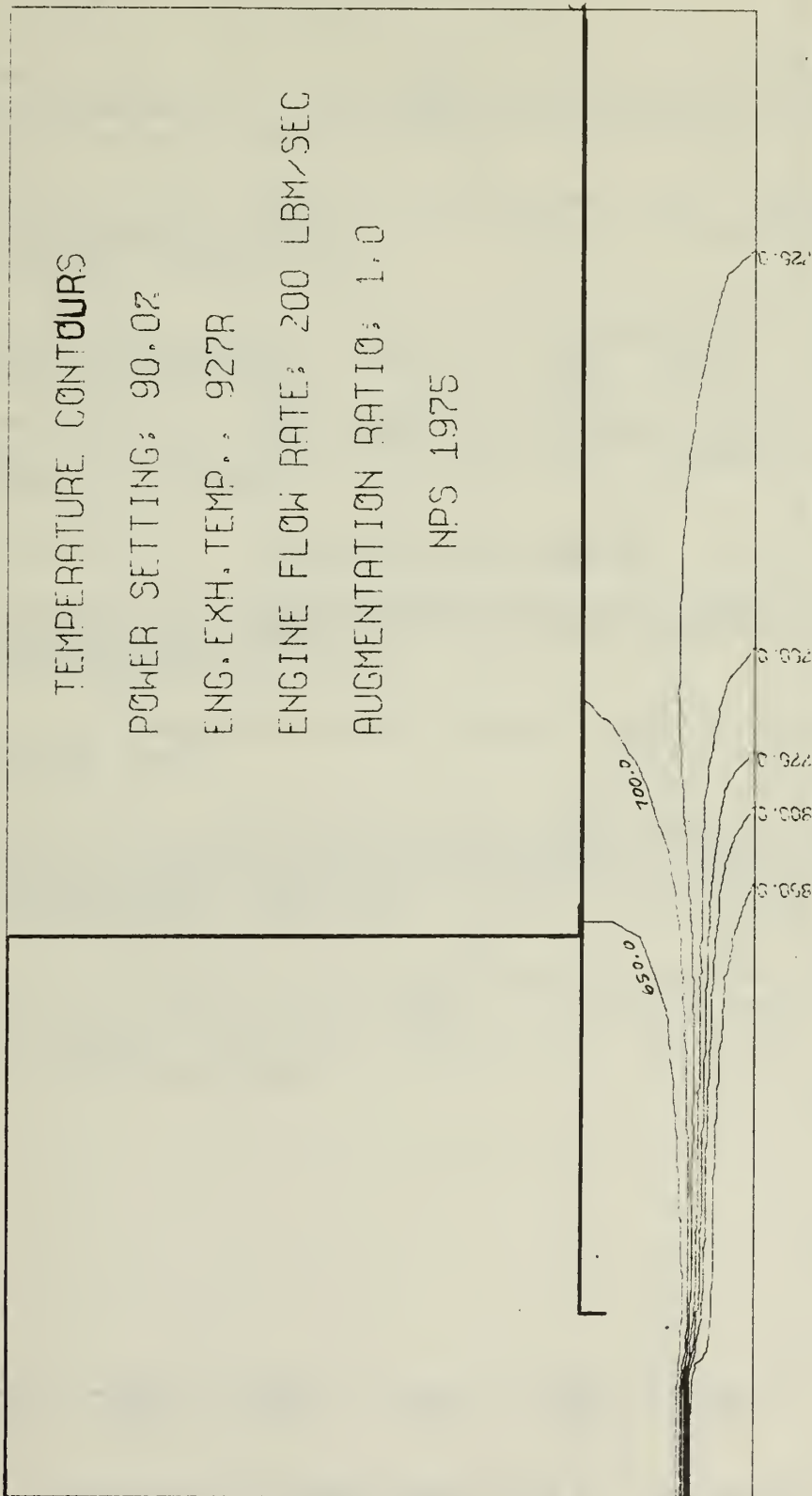


FIGURE 13b. TEMPERATURE CONTOURS: FLOW CONDITION 6

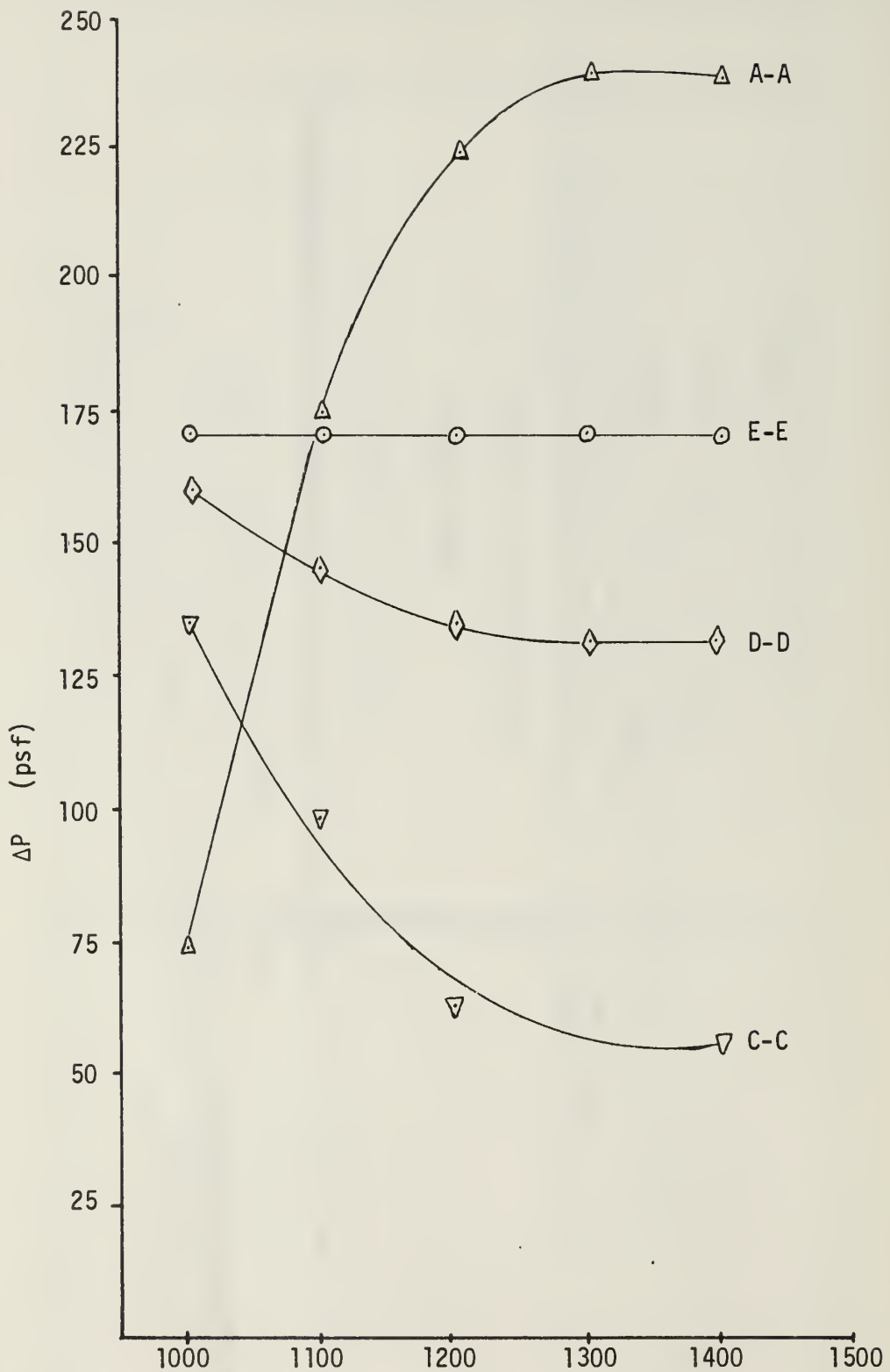


FIGURE 13c. ΔP RISE VERSUS NUMBER OF ITERATIONS:
FLOW CONDITION 6

LIST OF REFERENCES

1. Gosman, A.D., Pun, W.M., Runchol, A.K., Spalding, D.B., and Wolfshtein, M., Heat and Mass Transfer in Recirculating Flows, Academic Press, 1969.
2. Spalding, D.B., Gosman, A.D. and Pun, W.M., The Prediction of Two-Dimension Flows, Short Course, Pennsylvania State University, August 1972.
3. Launder, B.E., and Spalding, D.B., Lectures in Mathematical Models of Turbulence, Academic Press, 1972.
4. Speakman, G.C., Flow Field Calculations in Turbojet Test Cells, M.S. Aero. Eng. Thesis, Naval Postgraduate School, Monterey, California, June 1975.
5. Schlichting, H., Boundary-Layer Theory, McGraw-Hill, 1968.
6. Wolfshtein, M., Convection Processes in Turbulent Impinging Jets, Imperial College Mechanical Engineering Department, SF/R/2, 1967.
7. Naval Air Rework Facility Alameda, Test Procedures: TF-41 Turbofan, 1974.
8. Bailey, D.L., An Analytical and Experimental Analysis Affecting Exhaust System Performance in Sea Level Static Jet Engine Test Facilities, Ae.E. Thesis, Naval Postgraduate School, Monterey, California, December 1972.
9. Advisory Group for Aerospace Research and Development Report 125, "Pollution Control of Airport Engine Test Facilities", by Lt. D.L. Bailey, Lt. P.W. Tower, and Professor A.E. Fuhs.

DISTRIBUTION LIST

	No. of Copies
1. Library Code 0212 Naval Postgraduate School Monterey, CA 93940	2
2. Department of Aeronautics Code 57 Naval Postgraduate School Monterey, CA 93940 Prof. R. W. Bell, Chairman Prof. D. W. Netzer	1 10
3. Defense Documentation Center Cameron Station Alexandria, VA 22314	2
4. Dean of Research Naval Postgraduate School Monterey, CA 93940	1
5. Dept. of the Air Force Air Force Weapons Laboratory Kirtland AFB, New Mexico 87117 (Attn: Environics Branch)	1
6. Chief of Naval Operations Navy Department Washington, DC 20350 (Attn: Codes: OP451, OP-453, OP987T1)	1
7. Chief of Naval Material Navy Department Washington, DC 20360 (Attn: Codes: 0341, 044P)	1
8. Naval Facilities Engineering Command 200 Stovall Street Alexandria, VA 22332 (Attn: Codes: PC-4, 03, 032B)	1
9. Naval Construction Battalion Center Port Hueneme, CA 93043 (Attn: Codes: 25, 251, 252)	1
10. Bureau of Medicine and Surgery Navy Department Washington, DC 20372 (Attn: Code: BUMED 5622)	1

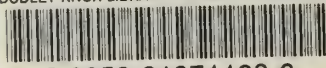
	No. of Copies
11. Navy Environmental Health Center 333 Vine Street Cincinnati, OH 45220 (Attn: Code: 1)	1
12. Navy Sea System Command Headquarters Washington, DC 20362 (Attn: Code: 03311)	1
13. Naval Ship Research and Development Center Annapolis, MD 21402 (Attn: Code: 2852)	1
14. Naval Air Systems Command Washington, DC 20361 (Attn: Codes: 01B, 340E, 330D, 4147A, 536B1, 53431B)	1
15. Naval Air Rework Facility Naval Air Station North Island San Diego, CA 92135 (Attn: Code: 600.1)	1
16. U.S. Marine Corps Washington, DC 20380 (Attn: Code: AAJ)	1
17. Naval Weapons Center China Lake, CA 93555 (Attn: Codes: 4503R, 70305)	1
18. U.S. Air Force Washington, DC 20330 (Attn: Codes: PREV 5E425, PREV 5D438)	1
19. Air Force Aero Propulsion Laboratory Wright-Patterson Air Force Base, OH 45433 (Attn: Code: SFF)	1
20. Air Force Civil Engineering Center Kirtland AFB, NM 87117 (Attn: Code: OL-AA)	1
21. School of Aerospace Medicine Brooks AFB, TX 78235 (Attn: Code: VNL)	1

	No. of Copies
22. Army Aviation Systems Command P. O. Box 209 St. Louis, MO 63166 (Attn: Code: EFP)	1
23. Eustis Directorate USA AMR & DL Ft. Eustis, VA 23602 (Attn: Code: SAVDL-EU-TAP)	1
24. National Aeronautics and Space Administration Lewis Research Center 2100 Brookpark Road Cleveland, OH 44135	1
25. Environmental Protection Agency Procedures Development Branch 2565 Plymouth Road Ann Arbor, MI 48105 (Attn: G. Austin)	1
26. Environmental Protection Agency National Environmental Research Center P. O. Box 15027 Las Vegas, NV 89114 (Attn: Code: MAL, Roy Evans)	1
27. Department of Transportation Transportation Systems Center Cambridge, MA 02k42 (Attn: Code: TI (A. Broderick))	1
28. Federal Aviation Administration 800 Independence Avenue, SW Washington, DC 20590 (Attn: Code: RD723, K. Forney)	1
29. Federal Aviation Administration 2100 2nd Street Washington, DC 20591 (Attn: Code: ARD550, W. Westfield)	1
30. Environmental Protection Agency 401 M. Street, SW Washington, DC 20024 (Attn: G. Kittredge)	1

	No. of Copies
31. Environmental Protection Agency National Environmental Research Center Meteorology Laboratory Research Triangle Park Raleigh, NC 27711 (Attn: P. Humphry)	1
32. Federal Aviation Administration National Aviation Facility Experimental Center Atlantic City, NJ 08405	1
33. National Aeronautics and Space Administration Langley Research Center Hampton, VA 23365 (Attn: Mail Stop 217K, Dr. Levine)	1
34. Naval Air Propulsion Test Center Trenton, NJ 08608 (Attn: A. Klarman)	2

U170234

DUDLEY KNOX LIBRARY - RESEARCH REPORTS



5 6853 01071128 6

~~U1702~~